

Structural, Magnetic, and Photocatalytic Properties of La, Se Co-doped BFO Nanoparticles-based Hybrids



Muhammad Umar

MPhil Physics

NUST00000117077

Supervised by:

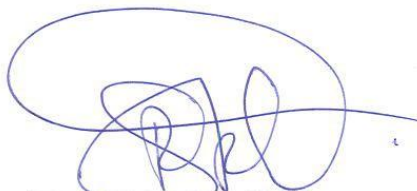
Dr. Syed Rizwan Hussain

(Associate Professor)

**School of Natural Sciences (SNS), National University of Science
and Technology, Islamabad (NUST) 2016**

National University of Sciences & Technology**MS THESIS WORK**

We hereby recommend that the dissertation prepared under our supervision by: Muhammad Umer, Regn No. 00000117077 Titled: Structural, Magnetic, and Photocatalytic Properties of La, Se Co-doped BFO Nanoparticles-based Hybrids be accepted in partial fulfillment of the requirements for the award of MS degree.

Examination Committee Members1. Name: Dr. Faheem AminSignature: 2. Name: Dr. M. Fahad EhsanSignature: 3. Name: Dr. M. Ali MohammadSignature: 4. Name: Dr. Farrakh ShahzadSignature: Supervisor's Name: Dr. Rizwan HussainSignature: 


Head of Department28/8/17


Date**COUNTERSIGNED**Date: 28/8/17


Dean/Principal

THESIS ACCEPTANCE CERTIFICATE

Certified that final copy of MS thesis written by Mr. Muhammad Umer, (Registration No. 00000117077), of School of Natural Sciences has been vetted by undersigned, found complete in all respects as per NUST statutes/regulations, is free of plagiarism, errors, and mistakes and is accepted as partial fulfillment for award of MS/M.Phil degree. It is further certified that necessary amendments as pointed out by GEC members and external examiner of the scholar have also been incorporated in the said thesis.

Signature: _____ 
Name of Supervisor: Dr. Rizwan Hussain
Date: _____ 28.08.17

Signature (HoD): _____ 
Date: _____ 28/8/17

Signature (Dean/Principal): _____ 
Date: _____ 28/8/17

All of My Work Is Dedicated To
My Loving Parents

“I couldn’t Have Done It Without Them”

Acknowledgement

All prays and glory is for **ALLAH** Whose worth cannot be described even by the greatest rhetoricians of all times, Whose blessings and bounties cannot be enumerated by beckoners and enumerators of all ages, and homage due to Him cannot be adequately paid even by the most assiduous and revering attempters.

It is my privilege to express my deep sense of gratitude to my research **supervisor, Dr. Syed Rizwan Hussain** for his constant persuasion, affectionate guidance and efficient supervision at each and every stage of this research work.

I am very grateful to the principle of School of Natural sciences **Prof. Dr. Azad Akhter Siddiqui** and Head of the Department of physics **Dr. Rizwan Khalid**, for their support and constructive suggestions. I would also like to thank my **GEC members Dr. Amin Faheem, Dr. M. Ali Muhammad** and **Dr. Muhammad Fahad Ehsan** for giving valuable guidance and suggestions to improve my thesis and research work; Many thanks to Dr. Qurat-ul-Ain for her continuous experimental support.

I would like to thank all the faculty members at SNS, non-teaching staff and my fellow students for the help provided to me at various stages to accomplish this research work.

Muhammad Umar

Table of Contents

| | |
|--|----|
| Abstract..... | 1 |
| Chapter 1: Introduction | 3 |
| 1.1. Introduction to Nanoscience..... | 3 |
| 1.2. History of Nanoscience | 3 |
| 1.3. Nanotechnology | 3 |
| 1.4. Nanomaterials..... | 3 |
| 1.5. Classification of Nanomaterials | 4 |
| 1.5.1 Zero Dimensional | 4 |
| 1.5.2 One Dimensional Nanomaterials..... | 4 |
| 1.5.3 Two Dimensional Nanomaterials | 4 |
| 1.5.4 Three Dimensional Nanomaterials | 5 |
| 1.6 What is important in Nanoscience?..... | 5 |
| 1.6.1 High Surface to Volume Ratio | 5 |
| 1.6.2 Quantum Confinement effect | 6 |
| 1.7 Types of Magnetic Materials..... | 6 |
| 1.7.1 Diamagnetism..... | 6 |
| 1.7.2 Paramagnetism..... | 6 |
| 1.7.3 Ferromagnetism and Ferrimagnetism..... | 6 |
| 1.7.4 Antiferromagnetism..... | 6 |
| 1.8 Multiferroic Materials | 7 |
| 1.8.1 Structure of BFO | 7 |
| 1.9 Applications of Nanotechnology..... | 8 |
| 1.9.1 Photocatalysis | 8 |
| 1.9.2 Energy..... | 8 |
| 1.9.3 Nanotechnology in Space | 9 |
| 1.9.4 Nanotechnology in Electronics..... | 9 |
| Chapter 2: Literature Review..... | 10 |
| Chapter 3..... | 18 |
| Synthesis and characterization techniques of Nanomaterials | 18 |
| 3.1. Approaches..... | 18 |
| 3.1.1. Bottom-up Approach | 18 |

| | |
|--|----|
| 3.1.2. Top down Approach | 18 |
| 3.2. Characterization Techniques | 19 |
| 3.2.1. Powder X-Ray Diffraction (PXRD)..... | 19 |
| 3.2.2. Scanning Electron Microscope (SEM) | 21 |
| 3.2.3. UV-Visible Spectroscopy | 24 |
| 3.2.4. Photocatalytic activity..... | 26 |
| 3.2.5. Vibrating Sample Magnetometer | 27 |
| 3.2.6. X-ray Photoelectron Spectroscopy | 28 |
| 3.3. Description of apparatus and method for synthesis | 29 |
| Chapter 4: Result and Discussion | 33 |
| 4.1. Result and Discussion of BFSO | 33 |
| 4.1.1. XRD Analysis of BFSO | 33 |
| 4.1.2. SEM Results of BFSO..... | 34 |
| 4.1.3. Magnetic properties of BFSO..... | 36 |
| 4.2. Result and Discussion of BLFSO | 39 |
| 4.2.1 XRD Analysis of BLFSO..... | 39 |
| 4.2.2. SEM Results of BLFSO | 40 |
| 4.2.3Magnetic properties of BLFSO | 42 |
| Chapter 5 Result and Discussion | 45 |
| 5.1. Photocatalytic Activity of Pure BLFSO..... | 45 |
| 5.1.2 Photoluminescence spectra of Pure Samples BLFSO..... | 47 |
| 5.2. Photocatalytic Activity of BLFSO/GO | 49 |
| 5.2.1 XRD of BLFSO/GO Nanohybrids | 49 |
| 5.2.2 SEM images of BLFSO Hybrids | 50 |
| 5.2.3 X-ray Photoelectron spectra of (BLFSO/Go) Nanohybrids..... | 52 |
| 5.2.4 Photoluminescence spectra of BLFSO/GO Hybrid Samples..... | 53 |
| 5.2.5 Photocatalytic activity of Hybrid Samples | 54 |
| References..... | 57 |

Abstract

Recently, research on Bismuth ferrite BiFeO_3 (BFO) nanoparticles is dominated because of their significant multiferroic, physical, chemical, magnetic and optical properties as compared to their bulk counter parts. Owing to their novel properties, these ferrites promise various significant applications such as magnetic shielding, transformers, magnetic recording heads as recording media etc. This work represents synthetic approach along with formation mechanism and characterization of BFO, Se-doped BFO (BFSO), La and Se co-doped BFO (BLFSO), and GO/(BLFSO). Low-dimensional BFO, BFSO, BLFSO and GO/BLFSO nanostructures with various morphologies were successfully prepared through sol-gel method. X-Ray diffraction (XRD) was used to investigate the crystallinity of prepared samples. By varying the concentration of rare earth metals, the size of nanostructure changes along with the change in their shapes. Changed morphologies of all samples with varying doping concentrations were observed by Scanning Electron Microscopy (SEM). X-ray photon Spectroscopy (XPS) was used to check the elemental composition. The magnetic and photocatalytic properties were plotted by getting the data. Study of magnetic properties of these particles revealed that BFSO and BLFSO move toward soft magnetic material by increasing the concentration of dopant materials. Study of photocatalytic of these particles revealed that BLFSO and GO/BLFSO show different behaviour. Photocatalytic properties of pure BLFSO are higher than the Hybrid GO/BLFSO. Our results presented here are useful for magnetic recording media for read and write purposes.

Layout of Thesis

The layout of this thesis is as follows:

Chapter 1

In this chapter, the general concept about nanomaterials is presented. Types of nanomaterials are discussed. A brief introduction to the multiferroic material and Structure of BiFeO_3 is explained.

Chapter 2

This chapter includes the literature survey, a brief introduction to the multiferroic material and rare earth metal is presented which was extended to the detailed literature review. Doping of different materials in BFO and their effects on structural, magnetic and photocatalytic properties is also explained in literature survey.

Chapter 3

The third chapter explains the types of approaches for nanomaterials synthesis and details the experimental techniques and methods used to prepare and analyze the nanomaterials.

Chapter 4

The fourth chapter contains structural and morphological analysis of BFSO and BLFSO nanomaterials. Magnetic properties of BFSO and BLFSO are thoroughly explained as well.

Chapter 5

The fifth chapter comprised of the structural and morphological study of GO/BLFSO nanocomposites. The photocatalytic properties of pure BLFSO and GO/BLFSO are thoroughly explained.

Chapter 1: Introduction

1.1. Introduction to Nanoscience

Nanoscience is compound word having two parts, nano and science. Nano is a pre referring to 10^{-9} , it refers specifically to nanometers. Therefore, nanoscience deals with the objects in size regime of nanometer. It is an interdisciplinary field and it involves merger with other sciences such as physics, chemistry, etc [1].

In this size regime, matter exhibits unusual properties, which makes this science unique. The variation of properties as a function of size occurs in different materials differently [2].

1.2. History of Nanoscience

Richard Feynman first time gave the idea of nanoscience in 1959 during one of his lectures. He gave a concept “there is a plenty of room at the bottom” in his lecture presented in the conference of the American physical society.

Later on in 1974 N.Taniguchi used the word “Nanotechnology” for the first time at the international conference in Tokyo [3].

1.3. Nanotechnology

This is a technology that using objects or structures or phenomena at the nanometer scale. Nanotechnology is applicable to physical, chemical, biological system in order to explore the properties arising at the nano scale.

This new emerging technology has many different applications in the fields of energy devices, artificial intelligence, inexpensive space travel, biological medical research, medical etc [4].

1.4. Nanomaterials

These are the materials of intermediate size between molecular and macroscopic. A nanometer is one millionth of a millimeter. These materials have in the range of less than 100nm. Generally, this incorporates the studies the morphological characteristics of the materials that entail the nonometric scale [5]. Nanomaterials show different optical, magnetic, electrical, and other properties.

1.5. Classification of Nanomaterials

Following are the main types of nanomaterials;

- 0- dimensional
- 1- dimensional
- 2- dimensional
- 3- dimensional

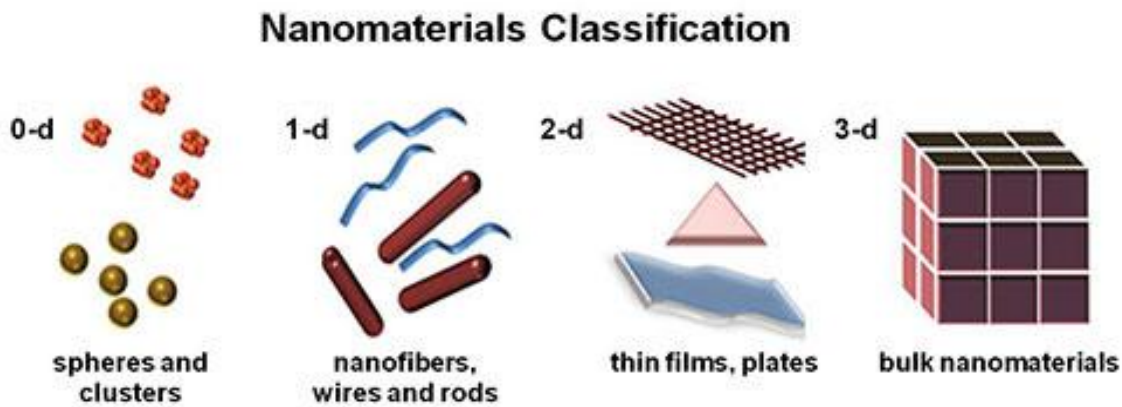


Figure1 Classification of Nano materials [6]

1.5.1 Zero Dimensional

These materials have all three dimensions limited in the nanoscale range and their size lie between 1nm to 100nm. The reduction of the size of the material gives rise to different characteristics. The examples of nanomaterials include nanoparticle, quantum dots and nanocluster [7].

1.5.2 One Dimensional Nanomaterials

Those types of nanomaterials in which the confinement is in two dimensional and only one dimension lie outside the nanoscale are called one dimensional nanomaterial. These contain nanorods, nanowires and nanotubes etc.

1.5.3 Two Dimensional Nanomaterials

Those type of nanomaterials in which two of the dimensions are not confined to nanoscale. Nanofilms, nanolayers and nanocoatings are the examples of these materials. These

nanomaterials can be made by various chemical compositions. These contain nanosheets, nanofilms etc. [8].

1.5.4 Three Dimensional Nanomaterials

These materials are not confined in any dimensions to nanoscale. These materials have three arbitrary dimensions above 100nm. They can be composed of multi nanolayers, nanowires, nanoparticles. These contain dendrimers, composites etc [9].

1.6 What is important in Nanoscience?

At nanometer scale, materials exhibit different properties not seen on a macroscopic scale. The following effect can change the properties of materials

1.6.1 High Surface to Volume Ratio

As we go down to smaller scale, surface area becomes larger as compared to its volume. In nanoscience this high surface to volume ratio is a very vital characteristic. Nanoscale particles have large surface area that maximizes possible reactivity. This large surface area to volume ratio is very effective in different chemical process and in making various materials. In convention materials most of the atoms are not at the surface. The large surface to volume ratio causes the chemical interactions to occur more easily. They can serve as very potent catalyst [10].

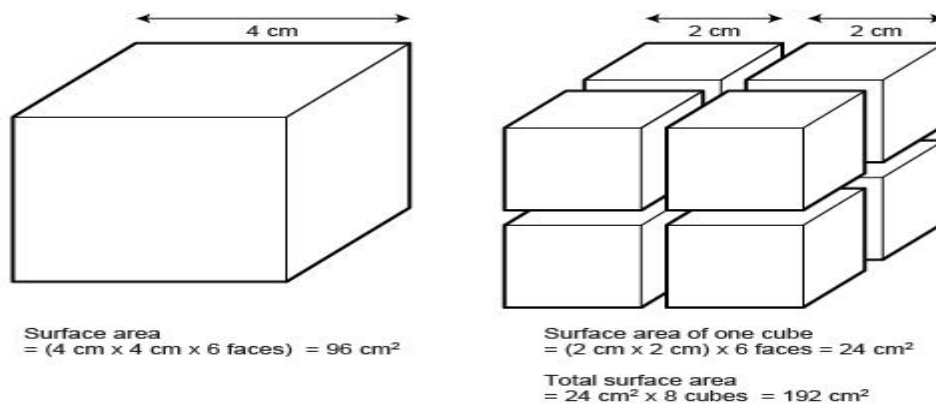


Figure 2 Presentation of high surface to volume ratio [11]

1.6.2 Quantum Confinement effect

The quantum confinement effect also plays a key role at nano scale. The word confinement corresponds to the limitation of the motion of electron to specific energy level and quantum reflects the atomic realm of particle [12].

1.7 Types of Magnetic Materials

1.7.1 Diamagnetism

The orbital motion of the electrons is the main source of Diamagnetism. The atoms that have completely filled orbital show this type of weak magnetic behavior. When this material is kept under the external magnetic field, a field opposite to the applied field is generated due to the orbital motion of electron, described by the negative susceptibility [13].

1.7.2 Paramagnetism

Paramagnetic behavior is observed in those atoms that show partially filled orbital. The presence of the dipole moment is because of the partial cancellation of electronic spin. Dipole moments are oriented arbitrarily before the applied field and they orient along the direction of the external magnetic field when field is applied. Thus, the material shows no net macroscopic magnetization. [14].

1.7.3 Ferromagnetism and Ferrimagnetism

Both these types of magnetic material shows permanent magnetic moments even when no magnetic field is applied. The cooperative interactions of atomic spins called domains regions are the source of permanent magnetic moment and these are the main source of magnetic behavior in ferromagnetic materials. In domain region all spins have the same direction. In ferrimagnetic materials these domains are oppositely aligned and do not show complete cancelation. The macroscopic magnetization in ferromagnetic and ferrimagnetic materials is the sum of the magnetization of the domains [15].

1.7.4 Antiferromagnetism

In these materials, the magnetic moments are due to the spins of electrons. In these materials domains spins are pointing in opposite directions [16]. Generally, antiferromagnetic order may exist below a certain temperature and vanishes at the Neel temperature.

1.8 Multiferroic Materials

Multiferroic materials exhibit simultaneously both ferroelectric and magnetic properties. These materials have two of the major ferroic properties in the same phase. Ferromagnetism, ferroelectricity, ferroelasticity and ferrotoroidicity are the main primary ferric orders [17].

In multiferroic materials, magnetic order is basically originated from the interactions among the magnetic dipoles due to the unfilled shells of electronic orbital. Electric ordering is due to the local dipoles, elastic ordering originates as a result of atomic displacement due to strain. These simultaneous presences of electric and magnetic ordering make these materials interesting as they contain combine properties of electric and magnetic properties. The best known examples of multiferroic materials are BiFeO₃, MnFeO₃ etc.

1.8.1 Structure of BFO

BFO is an important multiferroic material that shows both high T_C of about 1103K and T_N at 643k. BFO have rhombohadrally distorted Perovskite like structure with space group R3C. The formula of perovskite structure is ABO₃ in which A, B are cation and O anion oxygen which are located at the octahedral site of the lattice [18]. BFO is G type antiferromagnetic. In BFO both ferroelectricity and magnetic behavior exists. Ferroelectricity is due to the 6s² lone pair electrons of Bi⁺³ions and magnetic behavior arises due to the Fe⁺³ ions [19].BFO shows spin cycloid structure with period of 62nm [20].

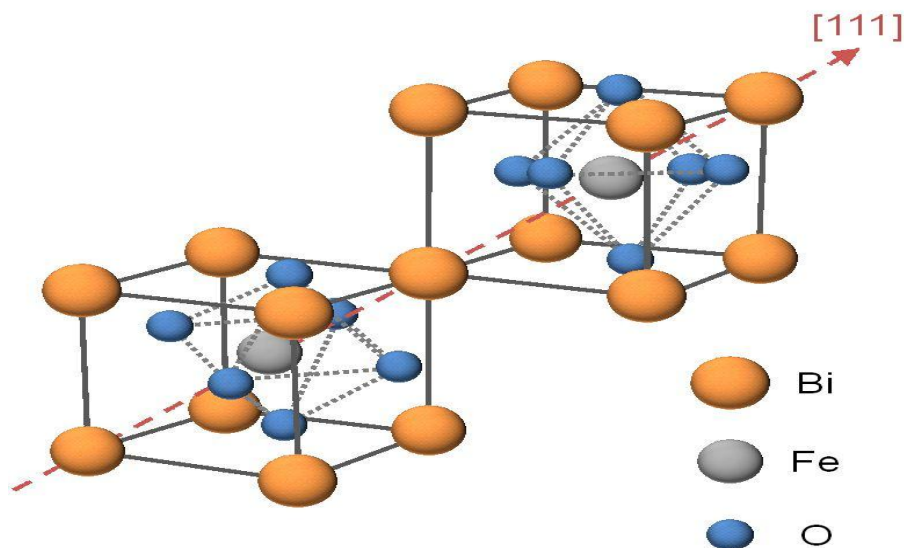


Figure3 Crystal structure of BFO [21]

When BFO is deal at nano scale there is optical and magnetic properties changes .The Neel and Curie temperature decreases with decreasing the nanoparticles size of BFO. While the value of magnetization value increases in nanoparticles, nanowires and in nanostructures because of the high surface to volume ratio at nano scale and cause the uncompensated spins at surface that increases magnetization value. For small particles the surface spins increases and increase in magnetization value [22].

1.9 Applications of Nanotechnology

Nanoamterials cover large range of applications due to their unique and useful properties. Some of the applications are discussed below

1.9.1 Photocatalysis

Photocatalysis is the acceleration of photoreaction in the presence of catalyst. Nano materials have got a great importance in this field because nanomaterials have large surface to volume ratio, so they can easily react fast and increase the reaction rate.

- Different metal oxides i.e. TiO_2 , ZnO , SnO_2 and CeO_2 , which are abundant in nature, have been extensively used as photocatalysis, particularly as heterogeneous photocatalyst since several decades.
- Literature shows that TiO_2 nanotubes are used for photocatalytic applications.
- Using the nanohybrid materials, the efficiency of photocatalyst can be increased.

1.9.2 Energy

The energy related projects of the nanotechnology includes the storage, conversion, manufacturing improvements.

- By using the nanopoures filters, the pollutants of combustion engines are reduced to greater extent.
- Carbon nanotube fuel cells environmentally friendly form of energy and they are used in different applications.
- Nanotechnology has played indispensable rule in solar energy storage devices.

1.9.3 Nanotechnology in Space

Nanotechnology has also found its applications in space explorations i.e. reducing the amount of rocket fuel, lowering the cost of space travelling etc.

- By using the carbon base materials like carbon nanotubes, weight of the space ships can be reduced and its structural strength can be increased.
- Using the nanohybrid materials the efficiency of material use for space missions can be increased.

1.9.4 Nanotechnology in Electronics

Nanotechnology helped in achieving the micro processors, which are more efficient in terms of processing speed and processing power. The micro processors are now reduced to the 100 nm size. More improved and energy efficient display screens are another application of nanotechnology.

- Manufacturing the carbon nanotubes based transistor with dimensionality of only a few nano meters to improve their efficiency.
- Nano material based magnets are being employed in the electrical circuits to reduce the power consumption.

Chapter 2: Literature Review

V. Annapuv Reddy et al studied the dependence of magnetic properties on the particle size of BFO_3 nanoparticles. How the magnetic properties change as the particle size change. From 10-150 nm was studied. BFO_3 nanoparticles with different size ranges were prepared by using the spray pyrolysis method. The crystal structure was confirmed by XRD and the FTIR spectroscopy analysis. Morphological studies were done by the SEM and SEM images showed the uniform and homogenous distribution of particles of different sizes. The significant increment in the value of magnetization and change in coercivity was reported as the particle size goes to nano scale. It is reported that the existence of spin cycloid structure is because of the large un-compensation of Fe^{+3} spins at the particle's surface. The phase transition have been investigated and reported that the Neel temperature and Curie temperature increases with particle size. The correction length, dimension and particle size provide more physical studies in the nanoparticles samples. The enhanced magnetic properties in smaller particles are caused by the spin cycloid structure's suppression [23].

Tae-Jin Park et al in 2007 reported the magnetic properties of crystalline BFO_3 nanoparticles with different sizes. For the synthesis of single crystal BFO_3 nanoparticles, facile sol-gel methodology based on glycol-gel reaction was used. The particle size between 10nm-100nm has been thermodynamically controlled. The morphological studies were done by the SEM. It is shown that the magnetic properties change with the change in particle size and this behavior is correlated (a) with decreasing nanoparticles size, suppression of spiral spin structure also increases and (b) existence of some uncompensated spins. ZFC and FC shows the different magnetic curves. The presence of insignificant Fe^{+2} causes oxygen deficiency. Oxygen deficiency causes the increase in multiferroic behavior [24].

R. Jarrier et al reported the surface phase transition in BFO_3 below room temperature. They used different techniques i.e. Resonant ultrasound spectroscopy, EPR, Raman spectroscopy etc to analyze the phase transition in bismuth ferrite at low temperature. It is reported that surface phase transition occur at $T=140.3\text{K}$ in BFO_3 with change in lattice parameters [25].

P Fischer et al explained that the crystal and magnetic structure of BFO_3 is also depends on temperature. The structure of BFO_3 was investigated by means of neutron diffraction on

powder sample. By change in temperature, distortion in the structure occurred and it is reported that the angle of oxygen tilts around the triad axis decreases from 12.45° at 4.5K to 11.4° at 878K. By increasing the temperature value, cation shifts also decreases. Changes of cation shifts, shift angle, distortion and strain octahedral look like the phase transition observed by Polomska [26].

BFO_3 has strong ferroelectric and magnetic properties simultaneously at normal room temperature. G Catalan and J F. Scott studied the Bismuth ferrite. It is reported that at some temperature phase of BFO_3 is called as rhombahedral with space group R_3C . In BFO the unit cell has a lattice parameter of 3.965 \AA . In BFO_3 , the rotation angle of oxygen and Fe-O-Fe angle are very important structural parameter. It was shown that as the size of BFO_3 change at nanoscale the magnetic hysteresis loop changes due to the partially compensated surface spins in BFO_3 nanocrystals [27].

Yongang W. et al reported the synthesis of single crystal bismuth ferrite nanoflakes by hydrothermal method assisted by KNO_3 . X-Ray diffraction and TEM are used for characterization. TEM images show the hydrothermal process at 200°C for different time i.e. 24h, 36h, 48h. By holding the sample for long time, the crystallites were made of the nanoflakes with the side length of 100-200 nm. The formation of nanoflakes can be described at the expense of nanoparticles. KNO_3 played a vital role in the formation of BFO_3 nanoflakes. This process is expected for the synthesis of nanostructure with different morphology [28].

Sushmita Gosh et al used ferrioxalate precursor method for the formation of bismuth ferrite nanoparticles. In this method, BFO nanoparticles are synthesized in pure phase at temperature 600°C . The characterization techniques used are X-Ray diffraction, FTIR, SEM etc. The particle size (11-22 nm) of the powder was calculated by the Scherer's formula. Differential thermal analysis shows a phase change at 385°C temperature. Oxalic acid acts as the chelating agent in this synthesis method. This method is very useful for the formation of BFO_3 nanoscale powder at much lower temperature compared to other methods. In low temperature synthesis oxalic acid and nitric acid play a crucial role for the formation of BFO_3 [29].

Yonggang Wang et al also synthesized BFO nanoparticles at low temperature 160°C by the hydrothermal method assisted by polymer. The chemical reagents used were bismuth nitrate, iron nitrate, potassium nitrate, polyvinyl alcohol and potassium hydroxide. XRD analysis shows

the existence of pure BFO with a rhombohedrally distorted perovskite structure. TEM images shows the sample prepared at 160⁰C with and without addition of polymer BFO crystals were in the shape of cubic sugar and when polymer was added samples were in the shape of sphere-like particles. These studies show that polymer play an important role in morphology of BFO nanoparticles [30].

Chao Chen et al in 2006 reported low temperature hydrothermal synthesis for the formation of perovskite bismuth ferrite crystallites. Effect of temperature, KOH concentration the initial conditions on the size of particle and morphology was investigated. Crystal structure was confirmed by the XRD. Morphological studies were done by scanning electron microscope. SEM images show how different molar value of KOH i.e. 4M, 6M, 10M affects the morphology of sample. SEM images also confirmed the homogeneous distribution of crystallite [31].

CAO Ling-fei et al in 2007 explained that the Curie temperature is affected by the shape and size of nanoparticles. It was reported that spin interactions exist between surface atoms and inner atoms. When the size is decreased the interaction conditions also changes that affect the ferromagnetic properties. It is also reported that the shape of nanoparticles effects the critical temperature variation [32].

Ziang et al in 2012 reported that the optical and magnetic properties of Bismuth ferrite changed by the La doping. Crystal structure, magnetic properties and optical properties of BFO nanofibers due to La doping was investigated with different experimental techniques i.e. XRD, EDX, SEM and UV-visible spectroscopy. The XRD pattern shows that there is no prominent change in the structure of BFO before doping because La is doped on small level. The lattice constants of the crystal remain unchanged because the comparable size of La⁺³(1.032⁰A) and Bi⁺³(1.03⁰A). The magnetic analysis shows that by increasing the La concentration, at first the value of magnetization weakens but by increasing the La concentration, the value of magnetization increases. Magnetization and coercive field exhibit an uninterrupted increase as the La doping increases. The result of UV-visible tests exposed little influence of La doping on the optical property [33].

Poorva Sharma et al studied the effect of rare earth (La) and metal ion (Pb) substitution on the structural and magnetic properties of Bismuth ferrites Bi_{0.825}A_{0.175}FeO₃ (A=La, Pb) were synthesized by solid state reaction rout. Crystal structure was examined by XRD that reveals that

structure changes by doping of La and Pb. By doping of La and Pb at Bi site in BFO a change in Raman model position was observed from Raman scattering measurements. Magnetic properties changes differently with La and Pb doping. It is also reported that porous ceramics have lower value of dielectric constants and these are most useful electronic devices. [34].

Z. X. Change et al have also studied the effect of La doping in BFO. $\text{Bi}_{(1-x)}\text{LaFeO}_3$ ($x=0,0.1,0.2$, and 0.3) have been synthesized by solid state reaction. Different structural changes occur by different concentrations values have been studied by XRD. It is reported that below 10% the structure remains same but at 20% doping structure changes to orthorhombic and at 30% doping structure changes to tetragonal. From the electric polarization hysteresis loops, La doping notably reduces leakage current and leads to the observational of the electric polarization hysteresis loop. It was reported that La doping affects the cycloid spin structure and enhance the magnetic moment [35].

O. Garcia-Zaldivar et al reported the co-doping effect of Ba, La and Ti in BFO. They reported the co-doping effect on magnetic and structural studies. Solid state reaction was used to Bi based multiferroic system. Different properties i.e. structural and magnetic properties were studied at different temperature. For structural studies XRD measurements were done. Morphological studies for different concentration of dopent material was done by SEM. XRD results confirmed the improved rhombohedral phase stability of BFO. A decrease in grain size with dopent incorporation reduces the distortion in the structure. The increase magnetic properties were reported by La doping and oxygen vacancies were found via XPS measurements [36].

Syed Irfan et al reported the co-doping effect of La and Mn in BFO with enhanced photocatalytic activity. The technique used for the fabrication of this sample is double solvent sol-gel technique. The co-doped La and Mn in BFO gyroid-like mesoporous nanostructure was obtained by controlling the calcinations process and by the amount of precursor. The structural studies were done by XRD. Morphological studies were done by SEM and SEM images showed the well-ordered mesoporous nanostructures with different doping concentration in BFO. It is reported that the doping of La and Mn in BFO causes better photocatalytic performance. The BLFMO samples show the similar optical absorption behavior like BFO in UV region but show significantly higher absorption in visible range. Similarly the dye degradation rate under visible

light is higher than pure BFO. These highly porous and well-ordered nanostructure networks have many applications such as high photocatalytic applicability etc [37]

Ting diu et al synthesized successfully BiFeO₃ perovskite crystallites by using the sol-gel method using a PVA as the complexing agent. The initial ingredients used were iron nitrate and bismuth nitrates. The effect of the ratios of PVA (Mⁿ⁺/-OH) on the morphology of BiFeO₃ was examined. Different techniques were used i.e., X-rays diffraction, field emission, FTIR etc. It was studied that the single phase well crystallized BiFeO₃ was obtained from Mⁿ⁺/-OH = 2:1 at 400°C and with Mⁿ⁺/-OH = 4:1 at 600°C. Other ratios i.e., 1:1 and 1.5:1 didn't give the BiFeO₃. The crystal structure was confirmed by XRD. Thermogravimetry was used to analyze the BiFeO₃ powder. FTIR was used to determine chemical bonding BiFeO₃. Field emission studies elucidated that by increasing the temperature for 2:1 precursor ratios the particle size grows larger. [38]

Yuperg lvet et al reported the controlled morphology and visible light Photocatalysis activity of BiFeO₃ by using the solvents and surfactants. X-rays diffraction, scanning electron microscopy (SEM) and Raman spectroscopy are used for different characterization. For synthesis, different solvents and surfactants were used. De ionized water, ethylene glycol and monomethylethor act as solvent with different polarities. The CTAB and PED2000 were used as surfactants. XRD studies showed that samples prepared with deionized water have the strongest intensity peaks, demonstrating a well crystalline structure. XRD confirms the distorted rhomohadral R₃C structure of the samples. The intensity of peaks with other two solvents ethylene glycol and monomethylether are lower than deionized water peaks. These results indicate that polarity of solvent elicit a crucial impact on the quality of crystalline structure. SEM images depict that different shapes are obtained by using different solvent and surfactants i.e., in case of ethylene glycol solvent, most of the grains are round agglomerated, while monomethylether induced regular octahedron shape of particles. Different polarity solvent determine different reaction rate. The precipitates form different shape with different structure. Similarly surfactants have different polarities when added in the solution, they would absorb on different crystal face and cause different morphologies. FTIR studies show that the samples prepare in water and the sample shows the best photodegradation efficiency. When ethylene

glycol used as solvent, it shows minimum photodegradation. Similarly samples prepared with PEG-200 ranked are best in photocatalytic activity [39].

Yu-Jie Zhang et al in 2010 studied the different properties of BFO after doping of different elements in $\text{Bi}_{(1-x)}\text{R}_x\text{FeO}_3$ ($X = 1-0$, $R = \text{Sm, Eu, La, Nd, and Tb}$). X-rays diffraction shows the structural changes occur in BFO after doping. The literature shows that the A site and B site substitution in BFO with rare earth and transitional metals respectively changed the properties of BFO. BRFO was synthesized by utilizing the solid state reaction. Structural studies were carried out by XRD and it was shown as the value of doping concentration increased, structural transition occur from rhombahedral to orthorhombic between $x = 0.2$ and 0.4 . It is also shown that lattice constant decreases slowly as doping concentration increased, similarly unit cell's volume also changes. The unit cell volume of BRFO is smaller than BFO due to larger radius of Bi^{+3} than dopent radius. Magnetic studies show that by doping, the value of magnetization increased. The origin of enhanced M is due to the disturbing spiral magnetic ordering by doping. By increasing the doping concentration, both R-O distance and Fe-O distance changes, which enhance exchange interaction leads to increase in magnetization. Neel temperature value also changes due to doping. The T_N value increases by doping in BFO. This enhancement of T_N is the result of change in the Fe-O distance. The value of coercivity is also affected by the doping [40].

Zhiwu Chen et al in 2015 reported the ethylene glycol assisted hydrothermal method for the synthesis of pure BFO crystallized structure. BFO powder have been synthesized by using this method at the low temperature as 140°C . The initial ingredients used for this synthesis are bismuth nitrate, iron nitrate, ethylene glycol and potassium hydroxide. The successful formation of pure BFO perovskite was confirmed by XRD. XRD pattern also show that as the temperature increases impurity phase decreases and pure BFO phase greatly increases up to the value of 140°C . Ethylene glycol used as solvent plays a crucial role for the formation of bismuth ferrite. Ethylene glycol is used as solvent because it can avoid strong hydrolysis of bismuth cation and keep the different electronegativity of bismuth and iron. This also reduces the energy required to successful suspension and the formation of pure BFO phase. To determine the presence of elements on surface such as (Bi, Fe, and O) X ray photoelectron spectroscopy was done. The morphological studies were done by the scanning electron microscope. SEM images show that

the shape of BFO-EG microcrystal is nearly spherical with approximately size of 10 μm . Further magnification shows that the spherical structure consists of large amounts of small particles with average size 8-20nm. The magnetic studies were done by vibrating sample measurement technique. The magnetization curve shows that the ferromagnetic behavior with a good value of coercivity and saturation magnetization. UV-visible spectrum is discussed for BFO powders. BFO powder shows photocatalyst activity for degradation of organic compound [41].

Sunil Chuhan et al reported the effect of Ba doping in BFO and discuss how the structural, vibrational, optical and magnetic properties change by the doping. The method used for the synthesis $\text{Bi}_{(1-x)}\text{Ba}_x\text{FeO}_3$ ($x=0.05, 0.10, 0.15$) nanoparticles was sol gel method. Chemicals used in this method were bismuth nitrate, iron nitrate and barium nitrate. These materials were dissolved in deionized water. Structural studies were carried out by using the XRD. All XRD pattern shows the rhombohedral structure of highly crystalline BFO nanoparticles. The unit cell volume increases by doping the Ba in BFO. As the concentration of Dopent increases, unit cell volume also increases. The change in the unit cell volume is due to the different ionic radius of Ba and Bi. Also the bond lengths and angles Fe-O-Fe change by increasing the value of Ba. Morphological studies show that there is a change in morphology by increasing the concentrations of dopent materials. FTIR transmittance spectra are also discussed. Hysteresis loop shows that the value of magnetization increased by increasing of Ba value from 0.05 to 0.15. This increment in magnetization value is because of the effect of high surface to volume ratio. With decreasing the particle size, surface to volume ratio increase and anti ferromagnetic ordering interrupted and uncompensated spin cause the net magnetization [42].

Ping Tang et al synthesized $\text{Bi}_{(1-x)}\text{Gd}_x\text{Fe}_{(1-y)}\text{Mn}_y\text{O}_3$ by using sol gel technique. Different techniques like XRD, TEM, Raman spectroscopy, Uv-visible spectroscopy are used for the different characterizations. Single phase perovskite structure was confirmed by XRD. Results of Gd and Mn co doped BFO show that there exist two extra peaks representing the existence of orthorhombic phase. TEM images shows that particle are in the range of nanoscale. By increasing the concentration of dopent, the band gap of BGFMO changes. Mn doped BGFO nanoparticles show increases in magnetization up to optimal value of doping. The coercive force also changes by changing the concentration of Mn [43].

G.S Arya et al discussed the In and Co doped BFO and their enhanced magnetic properties at room temperature. They synthesized $\text{Bi}_{(1-x)}\text{In}_x\text{Fe}_{(1-y)}\text{Co}_y\text{O}_3$ ($0 < x < 0.1$, $0 < y < 0.05$) nanoparticles by combustion method. Co doping causes the distortion in the structure of BFO. XRD graphs show that some peaks merge into a single peak after doping. Some peaks merged and shift towards the higher diffraction angles because of the difference in ionic radii of In and Co in BFO. SEM images show the improve morphology in terms of porosity. The pores on the surface are due to the liberation of gas during the combustion method. TEM images of different size with different concentrations of doping are discussed. Co doping affects the electric and magnetic properties. It is discussed that doping at A and B site causes the difference in magnetic moment, which give rise to the net magnetization. But like magnetization, coercivity of all samples shows different behavior [44].

Chapter 3

Synthesis and characterization techniques of Nanomaterials

3.1. Approaches

Ultrafine dimensions of the order of 10^{-9} have been found in nanostructure materials. At this lower scale, several approaches may be implemented in the fabrication of the nanostructure material. Following two approaches are utilized for synthesizing of nano material and the manufacturing of nano structure in nanotechnology;

- Top down approach
- Bottom-up approach

3.1.1. Bottom-up Approach

The fabrication of nano material and nanostructures with the bottom up approach starts with single molecule, which are combined together in the form of: atom by atom, molecule by molecule or cluster by cluster. Different methods used in the bottom up approach are

- Co precipitation method
- Sol gel method
- Double solvent sol gel method
- Hydrothermal method.

3.1.2. Top-down Approach

The manufacturing of nanoparticles with the implementation of top down approach involves the construction of material by continues removal of material until required material is obtained by using the methods such as carving cutting, and molding. By applying these approaches, we succeeded to manufacture a range of machinery and electronics devices [45]. Following is a list of methods which are applied for the production of nano-scale materials

- Ball milling
- Nano-lithography

- Laser ablation

3.2. Characterization Techniques

Although, several techniques exist to characterize nano material but here, we utilized followings

- X-ray diffraction (XRD)
- Scanning Electron Microscopy (SEM)
- Vibrating Sample Magnetometer (VSM)
- Ultraviolet Visible Spectroscopy (UV-Vis)

3.2.1. Powder X-Ray Diffraction (PXRD)

PXRD deals with the identification of the crystalline specimen in their current phase as well as gives a structural analysis of unit cell dimensions. The analysis of crystalline specimens is performed in the uniform of the fine bulk powder. The principle of the PXRD technique is based upon the constructive interference of the crystalline structures of specimens and the monochromatic x-rays. The interaction of x-rays with the crystalline substance gives the XRD patterns.

Working Principle

When x-rays falls on an atom, then these rays reflect from the atoms of the materials almost in all directions and interference occurred. X-rays are produced in the x-ray tube source. The angle that is formed in result of incident x-ray with reference of diffracted x-rays gives the diffraction patterns [46].

Bragg's law

William Henry Bragg and William Lawrence Bragg initially proposed the idea of crystalline solids subsequent to their discovery of surprising pattern of X-rays reflection in 1913. At that time, it was a novel thing to know that at particular incident angles and wavelengths, crystals generate peaks of reflected radiation. The constructive interference of the scattered waves is obtained when the waves remain in phase after their reflection from crystals. When two waves undergo the interference phenomenon, their path difference is denoted by $2d\sin\theta$,

where θ is the angle at which scattering occurred. Bragg's law describes the condition for the constructive interference by the following relation

$$2d\sin\theta = n\lambda$$

n = positive integer

λ = incident wavelength

When the scattering angle satisfies Bragg's condition, an intense peak appears.

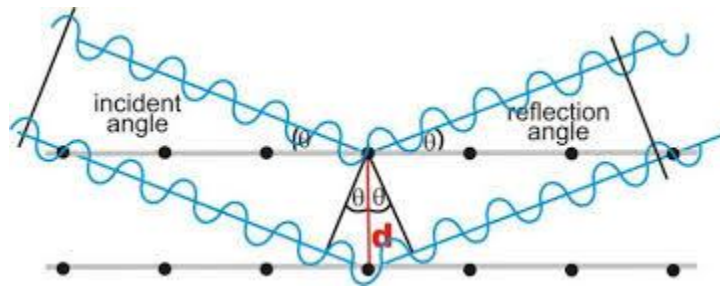


Figure 3.1 Bragg's Law [47]

Particle size can be measured by the Scherrer's formula given by the following equation

$$t = \frac{0.9\lambda}{B \cos(\theta_B)}$$

λ = incident wavelength

β = FWHM

Parts and working of PXRD

The components of powder x-ray diffraction machine are

- X-ray generation tube
- Specimen holder
- X-ray detector

The tube comprises of high-voltage tungsten filament cathode and copper anode. Large potential difference between anode and cathode fires the electrons to the target metal and generates the X-rays.

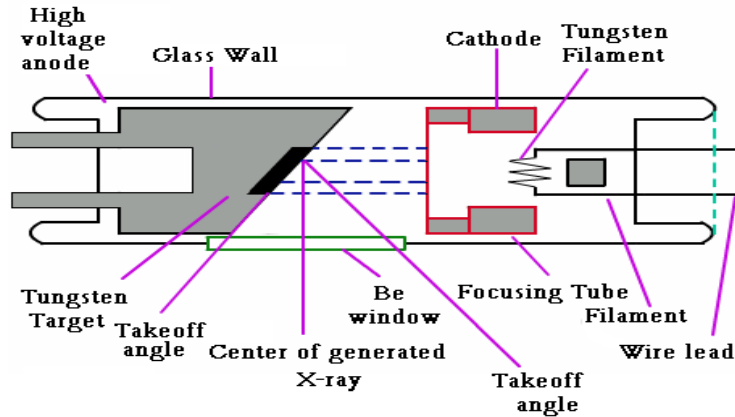


Fig 3.2 X-ray generation phenomena [48]

X-rays leave the tube via an exit window.

Applications

XRD is a nondestructive technique .It is used

- To identify crystalline phases and orientation
- To analyze the crystal structure
- To determine structural properties
- To determine atomic arrangement
- To detect the impurities present in the sample

3.2.2. Scanning Electron Microscope (SEM)

The morphological studies are performed by the scanning electron microscopy. A high-energy electron beam is thrown upon the surface the samples. The interaction of electron with the sample gives rise to different types of signals that give the morphological information of the sample. Magnification range 15x to 200,000x.This has the resolution in the range of angstrom Å. It has excellent depth of focus. It has relatively easy sample preparation.

Working of SEM

It contains the following parts

Electron Guns

The electron gun is placed either at bottom or at top of SEM and these guns shoot a beam of electrons at the object to be studied [49].

Condenser lenses

SEM uses these lenses to create comprehensive and thorough images. The lenses are not made up of glass but of electromagnetic material. These lenses are used to control and focus beam of electron to ensure their precise targeting.

Objective aperture

The objective aperture arm lie above the objective lens and it contain four holes. By the motion of the arm, different sized holes can be adjusted to put into the beam path.

Scan Coils

The scanning coils are basically the two solenoids that are used to create two magnetic fields perpendicular to each other. By varying the current, a magnetic field is generated that controls the movement of electrons.

Chamber

The sample chamber is a place where the specimen is kept for examining. By moving the chamber, different images are taken.

Detector

SEM contains various types of detectors. These detectors detect the various types of signals by the interaction of electron beam with the sample. Different types of detectors are backscattered electron detectors and X-ray detectors.

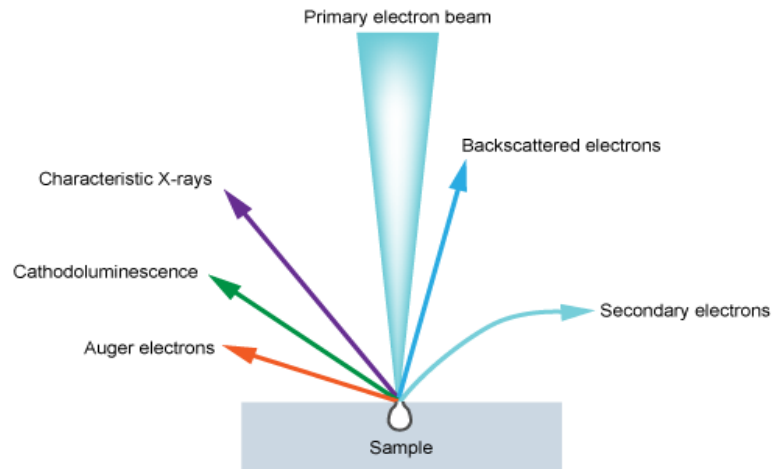


Figure 3.3 Radiation and electron in SEM [50]

There are different types of electron images.

- Secondary electrons emission
- Backscattered electron emission
- X-rays emission
- Electrons back scattered diffraction

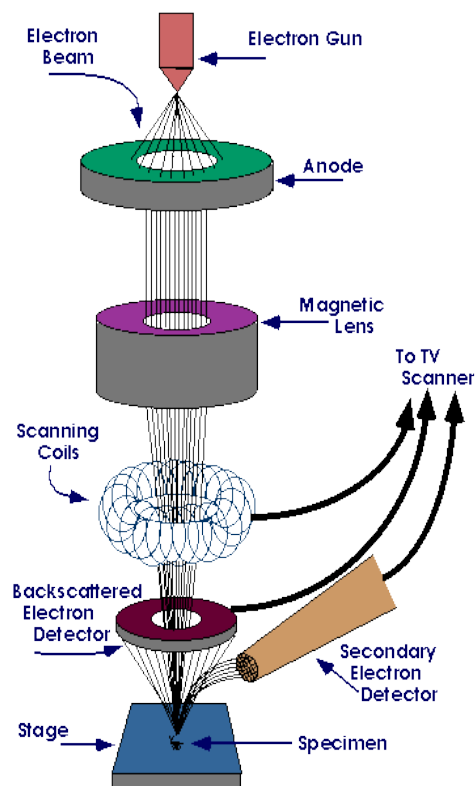


Figure 3.4 Construction of SEM [51]

Applications

- It is used for surface topography, morphology particle size etc
- It can be used for elemental maps or spots for rapid discrimination of phases in multiphase sample
- It is used for visualization of subsurface structure in cells and tissues
- SEM has particle applications such as semiconductor inspections
- It has technological application such as microchips for computer

3.2.3. UV-Visible Spectroscopy

UV-Visible spectroscopy is used to study the absorption spectrum, band gap studies etc. UV-visible spectroscopy is used to measure the absorption in both Ultraviolet (185-400nm) range as well as and visible (400nm-800nm).

Principle

It is the phenomena in ultraviolet and visible lights are used to measure the absorption calculations. In this technique, electronic transitions occurred due to the absorption of photon. It is type of Molecular Absorption Spectroscopy in which UV and Visible Radiations are used for quantitative and qualitative analysis. The wavelength range is from 200nm to almost 800nm. Spectrometer is used for the detection of those wavelengths at which absorption take place [52].

Beer-Alembert Law

This law basically gives the relationship of absorbance and molar absorptivity relating to UV-Vis spectroscopy. Mathematically it is described as

$$A = \log_{10}(I_0/I) = \epsilon cL$$

A = Absorbance

I_0 = Incident λ intensity

I = Transmitted λ intensity

L = Path length [53].

Instrumentation

The instruments used in this spectroscopy are as follow

1. Sources of UV-Visible light
2. Monochromator or Filter
3. Sample containers
4. Detector

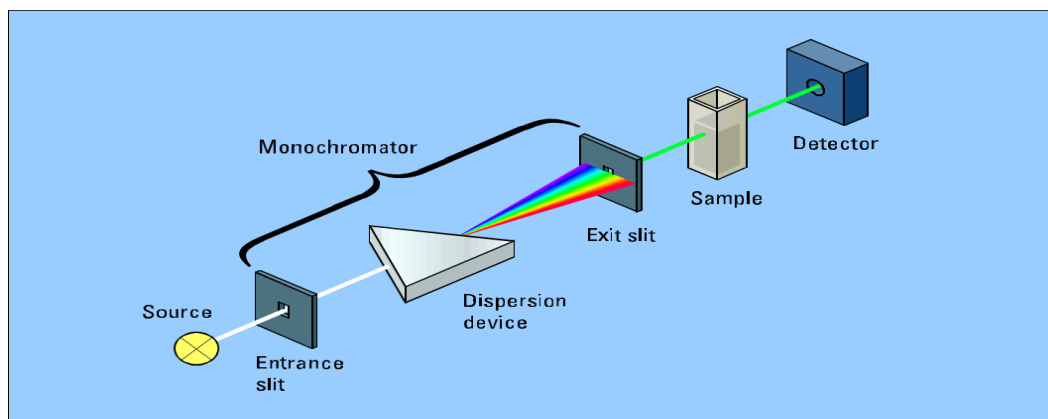


Figure 3.5 Representation of Experiment [54]

Applications of UV-Vis Spectroscopy

- Structure clarification of organic compounds
- Chemical kinetics
- Detection of Functional Groups

3.2.4. Photocatalytic activity

The photocatalytic activity is used to study photo-degradation of different organic dyes i.e. Congo red (CR), Methylene blue (MB), Methyl violet (MV) etc. The Photocatalytic degradation measurements are done by the UV-vis spectrophotometer (Hitachi UV-3310). For emission wavelength of 365 ± 5 nm as the UV light source a 5W LED and for visible light source with 420 nm and 800 nm a 300 W Xenon lamp were used as visible light sources. Approximately, 0.10 g photo-catalyst in powder form was added into 100 mL dyes solution in dark and stirred for 2h. Magnetic stirring and ice bath were given to avoid thermal effect during this degradation process. After that the solution was shown to the light source. During the photocatalytic reaction, 3 ml solution were removed periodically in every 30minutes, and centrifuged at 7000 RPM. The degradation rate depends on different parameters i.e. the structure of organic dye, light intensity, pH of the medium, illumination source, dye concentration, and catalyst morphology. The degradation efficiency of organic dyes is determined by using following formula,

$$\text{Degradation (\%)} = (C_0 - C_t) \times 100 / C_0$$

Here, C_0 represents the initial concentration of organic dye and C shows the final organic dye concentration degraded after the specified time interval. The absorbance spectra of CR solution were analyzed periodically by using a UV-*vis* spectrophotometer [55].

3.2.5. Vibrating Sample Magnetometer

The vibrating sample magnetometer is used for the study of magnetic properties of different magnetic materials. The Vibrating sample Magnetometer was first designed by Simon Foner, in 1959 at the Lincoln laboratories. It is used for magnetic measurements as a function of field and temperature of different magnetic materials.

Working principle and explanation

VSM working is based on Faraday's law of induction which states that a change in magnetic field will produce an electric field. This electric field gives information of magnetic behavior. The testing sample is kept in a sample holder which is kept between the pole pieces of an electromagnetic under a stable magnetic field. The sample is magnetized by aligning the domains in the direction of external magnetic field. A sample holder and a transducer are connected through vertical sample rod. The transducer converts the sinusoidal AC signal into vertical vibration and thus sample undergoes a sinusoidal motion in constant magnetic field. As the sample starts vertical motion, magnetic field in sample is varying and can be sensed by pick up coils. The change in magnetic field will generate an electric current in the pickup coils. This electric current is in proportion to the magnetization or magnetic moment of the testing sample. After this, induced current in pick up coils is amplified by a transimpedance amplifier [56]. The output is a hysteresis curve by analyzing the data. This curve gives the relationship between magnetizing force and magnetic flux density and gives important information about saturation magnetization, the remanence and coercivity.

Vibrating Sample Magnetometer Parts

- Power supply and water cooled electromagnet
- Sample holder and vibration exciter

- Sensor coils
- Amplifier
- Lock in amplifier
- Computer Interface



Figure 3.6 VSM image [57]

3.2.6. X-ray Photoelectron Spectroscopy

X-ray Photoelectron Spectroscopy (XPS) is used to study the chemical composition of different atoms on the surfaces.

Basic principle of XPS is photoelectric effect and it was developed in the mid of 1960 by Kai Seighbahn and his research group. Through XPS surface analysis can be performed and it can find elemental composition. The basic idea is that material is exposed to electromagnetic radiation usually in the form of X-ray. The incident photon has an amount of energy when hit to the electron in inner shell of atom, there will be ejection of electron called photoelectron. This ejected photoelectron has a kinetic energy. In this process there is also ejection of Auger electrons. XPS measure the kinetic energy of both photoelectron and Auger electron [58].

Instruments

- Electron energy analyzer
- X-ray source
- Ar ion gun

- Neutralizer
- Ultrahigh vacuum system
- Electronic controls
- Computer system
- Detection of electrons
- Avoid surface reactions/contaminations

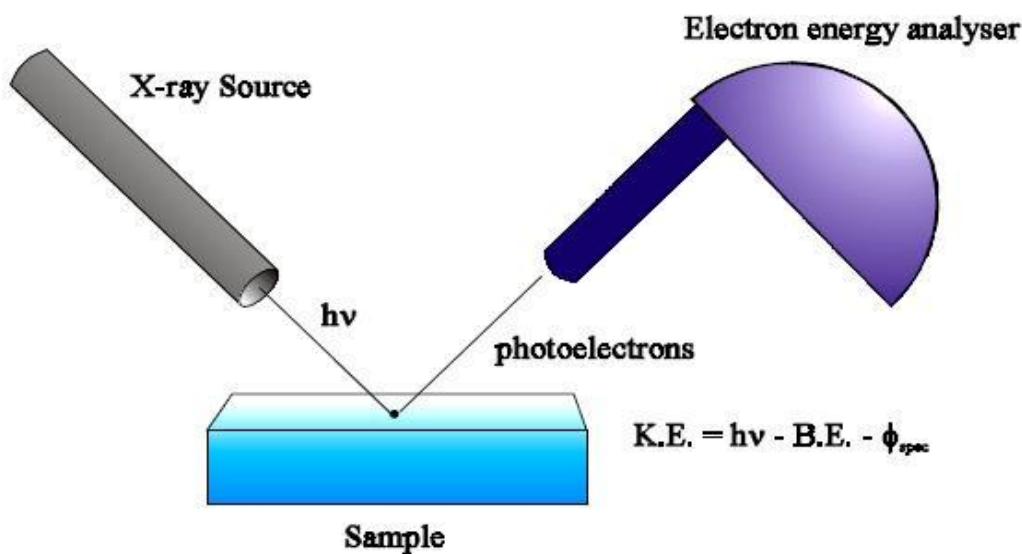


Figure 3.7 image of XPS [59]

Applications

- Use to find the chemical composition
- To find the empirical formula
- To find the electronic state of electrons

Description of apparatus and method for synthesis

The experimental work includes the synthesis method to prepare pure BFO (BiFeO_3), BFSO (Se doped BFO), BLFSO (La and Se doped BFO) nanoparticles, and BFSO and BLFSO hybrids with graphene oxide by double solvent sol gel method.

Equipment used

Following equipment are used for the synthesis of nanostructures through double solvent sol-gel method.

- Digital weight balance
- Magnetic hot plate
- Drying oven
- Muffle furnace
- Mortar and Pestle
- China Dish
- Centrifuge machine

List of chemicals used for synthesis

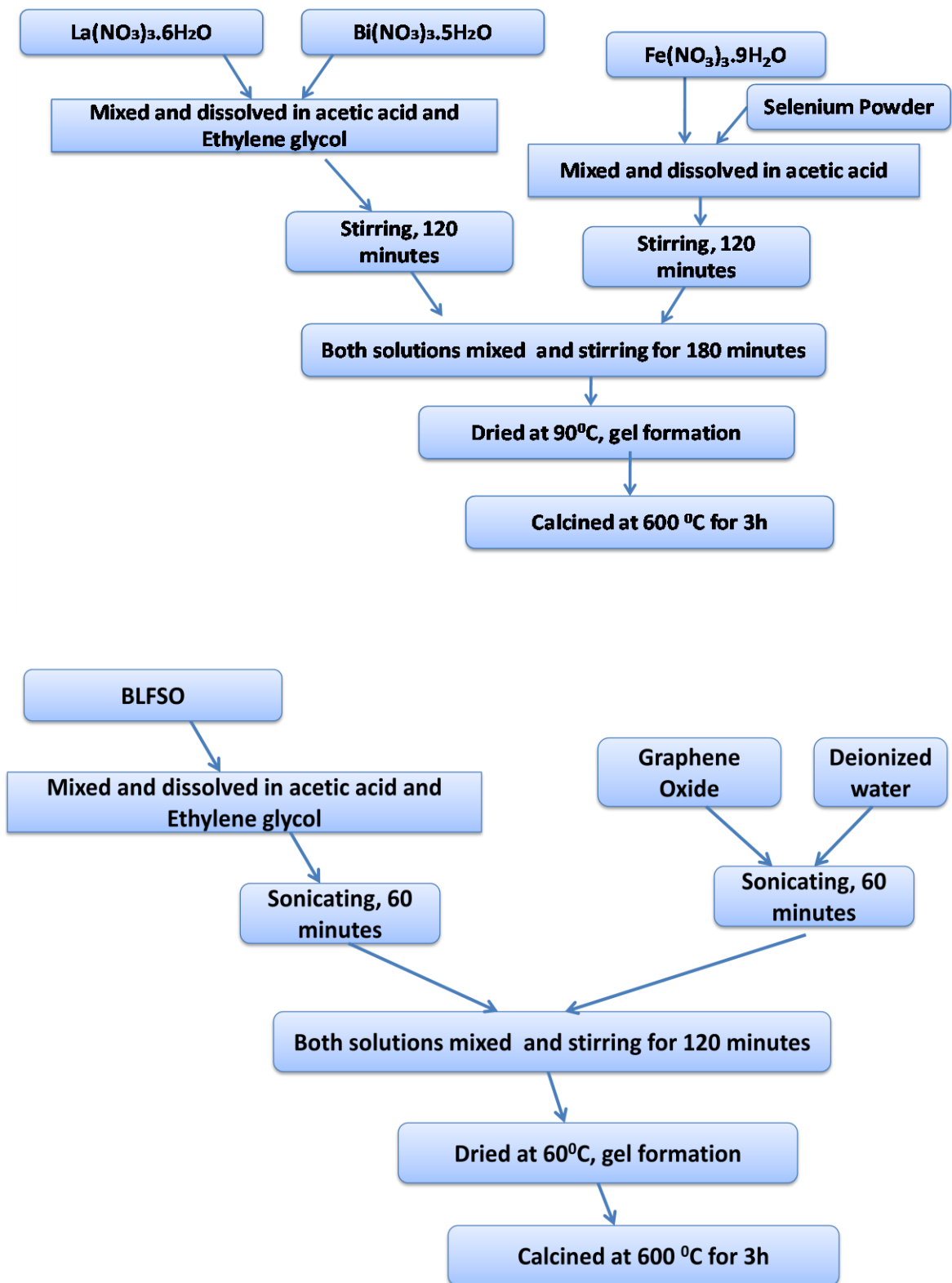
| Sr # | Chemical Name | Chemical formula |
|------|-------------------------------|--|
| 1 | Bismuth-nitrate pentahydrate | $\text{Bi}(\text{NO}_3)_3 \cdot 5\text{H}_2\text{O}$ |
| 2 | Iron nitrate nonahydrate | $\text{Fe}(\text{NO}_3)_3 \cdot 9\text{H}_2\text{O}$ |
| 3 | Selenium | |
| 4 | Lanthanum nitrate_hexahydrate | $\text{La}(\text{NO}_3)_3 \cdot 6\text{H}_2\text{O}$ |
| 5 | Ethylene glycol | $\text{C}_2\text{H}_6\text{O}_2$ |
| 6 | Acetic Acid | CH_3COOH |
| 7 | Graphene oxide | GO |
| 8 | Deionized water | |

Experimental Procedure

BFSO and BLFSO nanoparticles were synthesized by double solvent sol–gel technique. Briefly, $\text{Bi}(\text{NO}_3)_3 \cdot 5\text{H}_2\text{O}$ (99%, pure) and $\text{La}(\text{NO}_3)_3 \cdot 6\text{H}_2\text{O}$ (99%, pure) were stoichiometrically mixed and after mixing both these nitrates were dissolved in ethylene glycol [$\text{C}_2\text{H}_6\text{O}_2$] and acetic acid [$\text{C}_2\text{H}_4\text{O}_2$], and stirred for 2h at room temperature. On the other hand, $\text{Fe}(\text{NO}_3)_3 \cdot 9\text{H}_2\text{O}$ (98.5%, pure) and Selenium powder (Sigma Aldrich, 99.5% pure) were dissolved in acetic acid and stirred for 2h. Both above prepared solutions were again mixed and stirred for 3h on magnetic stirring. After that, solution was dried in an oven at 90 °C for 12h to get a gel and then calcined in furnace at 600°C for 3h [60].

The route employed in the present work is very simple. The hybrid of pure BFO, BSFO, $\text{Bi}_{1-x}\text{Sm}_x\text{Fe}_{1-y}\text{Mn}_y\text{O}_3$ nano particles with Graphene oxide were prepared by a Co precipitation method. In a typical synthesis approach, First of all prepare the solution of 10ml acetic acid and 10ml ethylene glycol in a beaker, and then add the required amount of Pure BFO into it. Put this beaker on sonicator for 60 min so that the BFO nano particles easily dispersed into the solution at room temperature. On the other side take another beaker, add deionized water and Graphene oxide into it according to the required amount and put it on sonicator for 60 min. After that, both solutions were mixed and stirring it for 120 minutes. Then brownish solution was achieved. To obtain a dry gel the as-prepared brownish solution was placed at 60 °C in an oven for drying. The obtained gel was calcined in air. The hybrid of all BFO doped samples with Graphene oxide were prepared by the same procedure. Here after the structural analysis of the all the BFO doped samples was done by X-ray Diffractometer (XRD) in the range of 20~80 using Cu-K α radiation. SEM was utilized for study the morphological analysis of all the prepared hybrids.

Flow chart



Chapter 4: Result and Discussion

4.1. Result and Discussion of BFSO

4.1.1. XRD Analysis of BFSO

Fig. 4.1 illustrates the XRD of pure BFO and Se⁺⁴ doped BFO, BFe_{1-x}Se_xO₃ (x=0.10, 0.25, .50 and 1.0) nanoparticles. XRD patterns matched exactly the typical peaks of Rhombohedral structure of pure BFO with space group R3c (JCPDS card no. 20-0169). From the XRD data, there is a peak shift related to the (104) and (110) planes towards the higher angles as we doped Se⁺⁴ in the sample. This peak shifting is due to the fact that the ionic radii of Se⁺⁴ (0.64 Å) and Fe⁺³ (0.78 Å) are not equal which causes change in the interplanar distance [56]. From the XRD data, it is clear that the dopant Se⁺⁴ moved the Fe atoms in BFO. Because of a large difference in the atomic radii of Bi⁺³ and Se⁺⁴, Se⁺⁴ cannot replace Bi⁺³. As we increase the concentration of Se⁺⁴, the peak near 2θ=39° becomes smaller and smaller which confirms the transformation in the rhombohedral structure to orthorhombic structure. There is also some impurity phase Bi₂₄Fe₂O₃₉ start to grow by increasing the value of dopant concentration. The Scherer formula is used to calculate crystallite size.

$$t = \frac{0.9\lambda}{B \cos(\theta_B)}$$

Where as

- 0.9= crystal shape factor
- λ= wavelength of incident X-Rays
- β= Full Width Half Maximum
- 2θ= Diffraction angle

The unit cell volume also decreases because the ionic radii of dopant material Se are less than the Fe ionic radii. This mismatch of iron and selenium cause the lattice strain inside the lattice which result in structural distortion and decrease in nucleation rate.

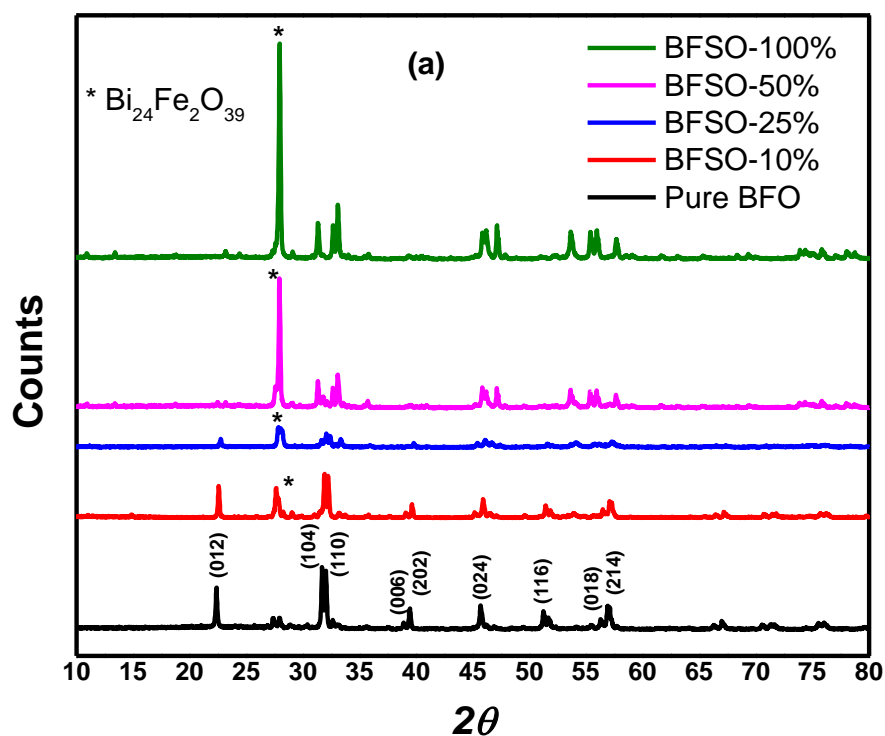
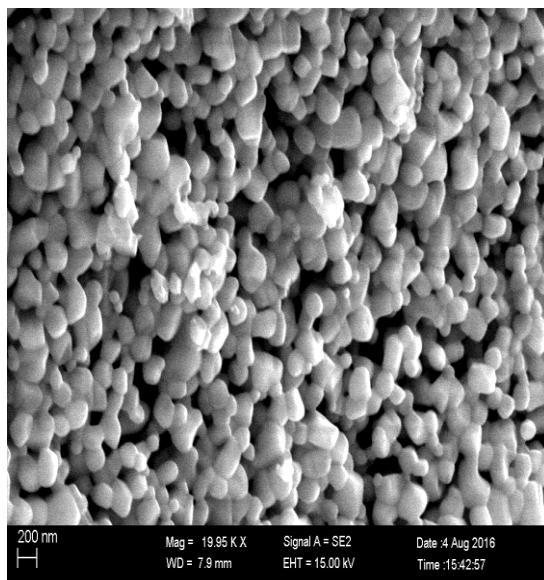


Figure 4.1. The XRD pattern of Se-doped BiFeO_3 at different concentration.

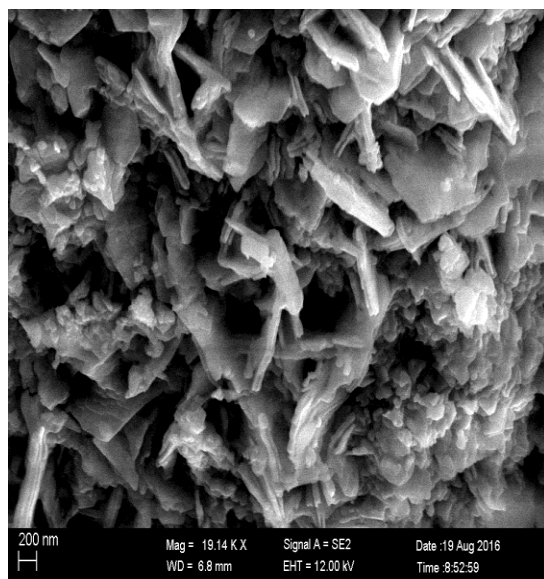
4.1.2. SEM Results of BFSO

Morphological analysis of BSFO nanostructure was done by using the scanning electron microscope (SEM) and is shown in Figures 4.2. SEM results show that the particle size and their shapes change by adding Selenium in the first sample, i.e. BSFO nanoparticles. The SEM images show that the shape of the nanostructure is continuously changed upon increasing the Se concentration. SEM images show a porous structure when only 10% of Se is added into the pure BFO nanoparticles and is changed to an intermediate phase consisting of porous nanoparticles, nano-needles and nanosheets formation when the Selenium doping is increased from 10% to 25%. In the third sample, the concentration of Se was increased to 50% and the shape of the nanostructure is almost shifted to pure nanosheets. Finally, when the concentration of Se is increased to 100%, the nanosheets are self-assembled in the form of a flower-like shape with nanosheets acting like the petals of the flower.

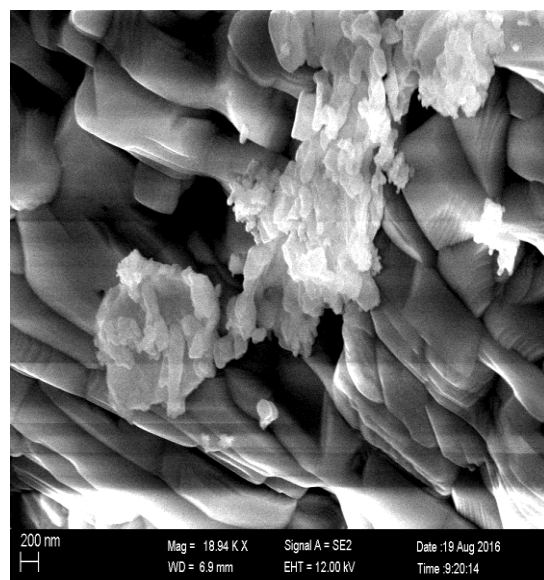
a) BFSO-10



b) BFSO-25



c) BFSO-50



d) BFSO-100

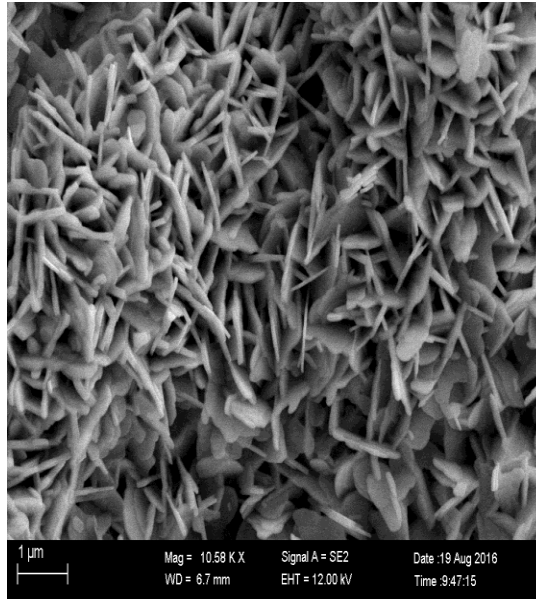


Figure 4.2. SEM images of (a) BFSO-10 (b) BFSO-25 (c) BFSO-50 (d) BFSO- 100.

4.1.3. Magnetic properties of BFSO.

Figure 4.3 shows the magnetization vs. magnetic field (M-H) curves for Se-substituted bismuth ferrite nanoparticles. The magnetic results show that for the first sample (BFSO-10), the magnetic moment of pure BFO changes from 0.052 emu/g to 0.0390 emu/g at room-temperature. The change in magnetization of the sample is because of the fact that the periodicity of the spin cycloid is destroyed at nanoscale and the uncompensated magnetic moments of the host and dopant atoms cause an increase in saturation magnetization. The net magnetization of the sample with Se=25% is increased to 0.0990 emu/g, much higher than the pure BFO sample. The origin of this enhanced magnetization with increasing Se concentration might be due to the distorted spiral magnetic ordering and is also due to the enhanced surface due to formation of the nanosheets [57]. When Se is added to BFO, the bond lengths between cations and anions change causing an enhanced spin interaction between core of the material. By increasing the concentration of Se above 25%, the saturation magnetization (M_s) behaves non-linearly and the value fluctuates. For final sample in which 100% Se is doped, the value of magnetization is only 0.0005 emu/g. These fluctuations are due to the continuous morphological effects which cause

change in shape of the nanostructures. The magnetization, remnant magnetization, and coercivity under the external magnetic field are given in Table 1, extracted from the M–H curves.

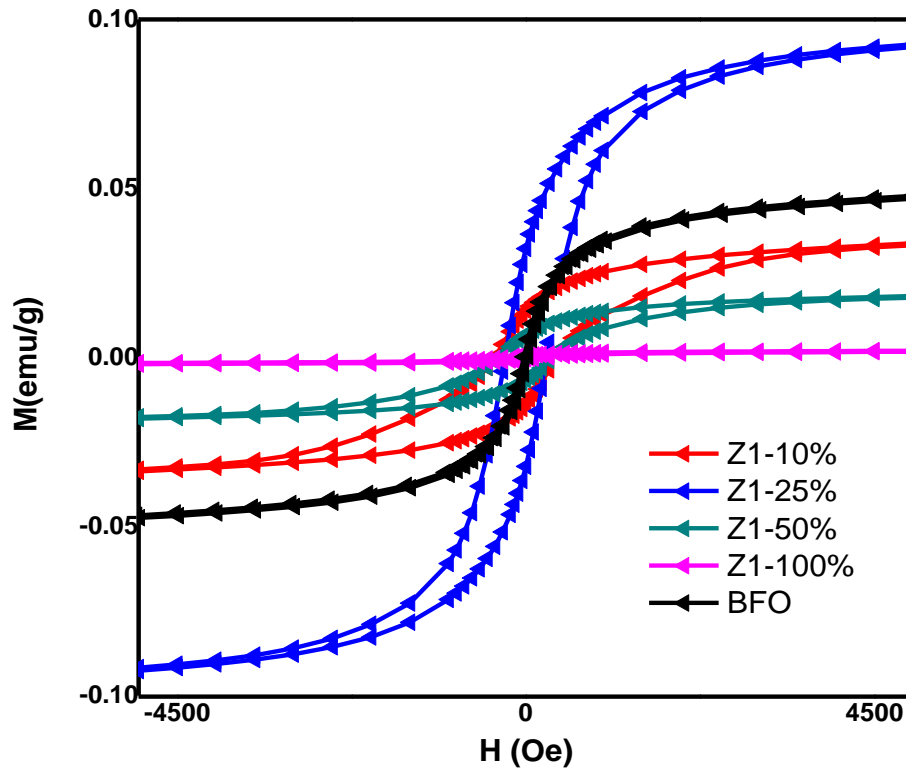


Figure 4.3. Magnetization vs. field curves for BFO plotted against different Se-%.

| Sample | Mr (emu ⁻¹) | Ms (emu ⁻¹) | Hc (Oe) | Mr/Ms |
|----------|-------------------------|-------------------------|---------|--------|
| BFSO-10 | 0.013 | 0.0390 | 410 | 0.33 |
| BFSO-25 | 0.034 | 0.0990 | 270 | 0.34 |
| BFSO-50 | 0.0072 | 0.0207 | 341 | 0.0347 |
| BFSO-100 | 0.0005 | 0.0025 | 250 | 0.02 |

Table 1. Table of magnetic parameters of Se substituted BFO.

Figure 4.4 shows the change in magnetic coercivity as a function of Se concentration. The coercivity of pure BFO is 22 Oe and the value of magnetization is 0.052 emu/g. For first sample in which Se=10 % is doped in BFO, coercivity increases to the value of 410 Oe. This increase in coercivity is due to the porosity of the sample as seen from SEM image a). For porous materials, there exist different magnetic regions that cannot be easily changed from their initial direction under an applied magnetic field. This results in the formation of more complex domain structure with smaller magnetic domains resulting in increase in the coercivity [58]. By increasing the concentration of Se (25%) in BFSO, the value of coercivity decreases from 410 Oe to 270 Oe. This change is attributed to the fact that the porosity of the material is decreased due to formation of partial nanosheets structure. At Se=50%, the coercivity increases from 270 Oe to 340 Oe due to the formation of complete nanosheets structure. This is due to the fact that magnetic domains become localized in the given shape boundaries and cannot be easily magnetize. The same irregular coercivity behavior goes to the last sample where Se=100 % owing to the flower-like nanostructure.

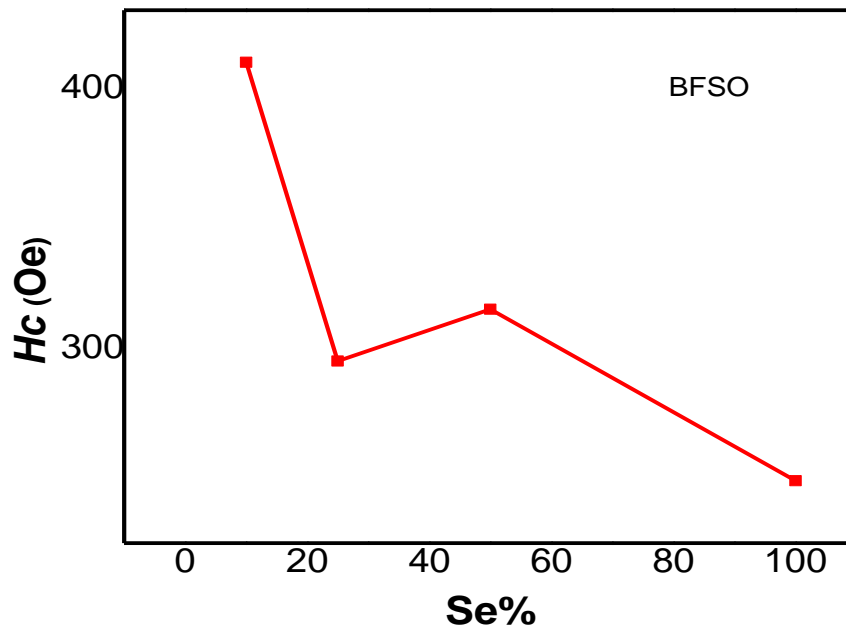


Figure 4.4. The magnetic coercivity vs. Se-concentration for BFSO.

4.2. Result and Discussion of BLFSO

4.2.1 XRD Analysis of BLFSO

Figure 4.5 illustrates the XRD of pure BLFO and Se^{+4} doped BLFO, $\text{B}_{0.92}\text{L}_{0.08}\text{Fe}_{1-x}\text{Se}_x\text{O}_3$ ($x=0.10, 0.25, .50$ and 1.0) nanoparticles. All the XRD match exactly according to JCPDS card no. 20-0169. From the XRD data, there is a peak shift related to the (104) and (110) planes towards the lower angles as we doped Se^{+4} in the sample BLFO. It is due to the fact that the ionic radius of dopent is different with the atoms of Bi and Fe. The intensity peak of (006) plane at 39° which arises from rhombohedral structure became weaker by increasing the Se concentration. This result showed the phase transformation from rhombohedral to orthorhombic phase. There is a detectable impurity peak of $\text{Bi}_{24}\text{Fe}_2\text{O}_{39}$ observed after doping of Se^{4+} . The impurity peak becomes sharper by increasing the concentration of Se above 25%.

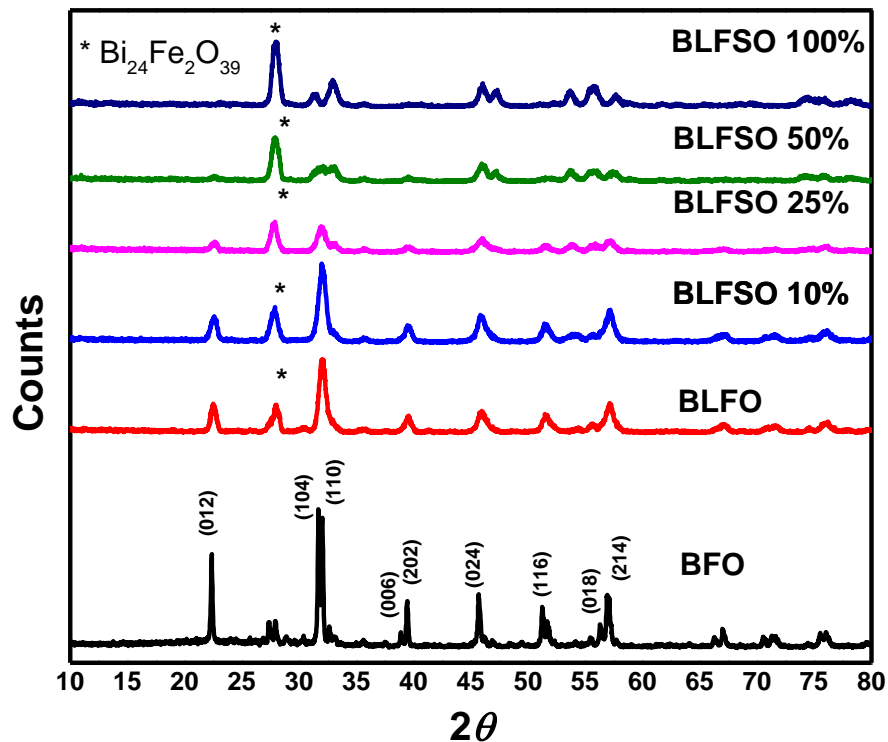
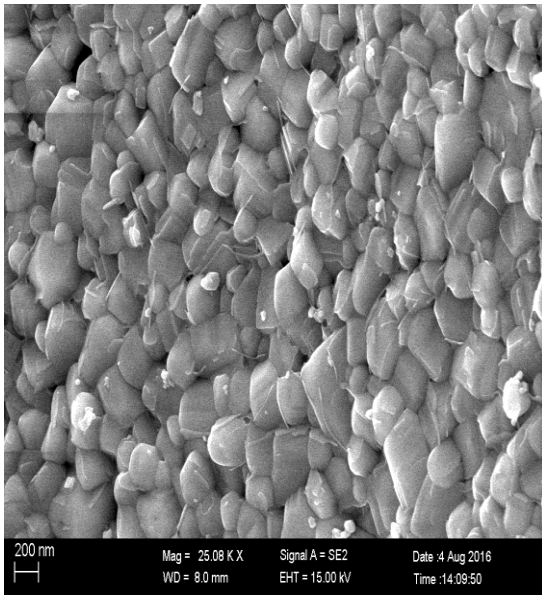


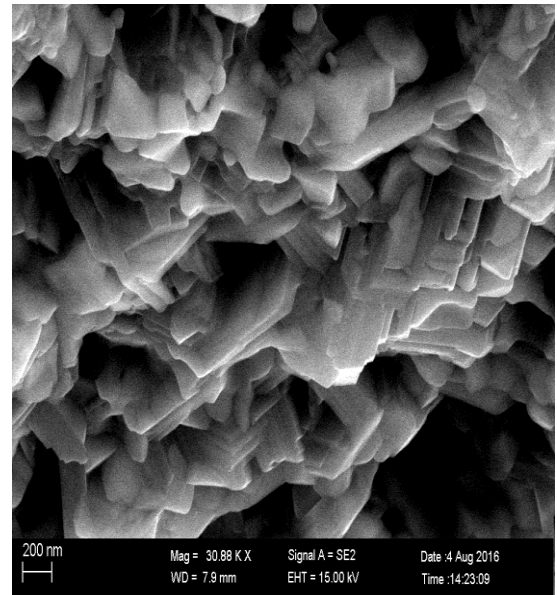
Figure 4.5. The XRD pattern of La, Se co-doped BiFeO_3 at different Se %.

4.2.2. SEM Results of BLFSO

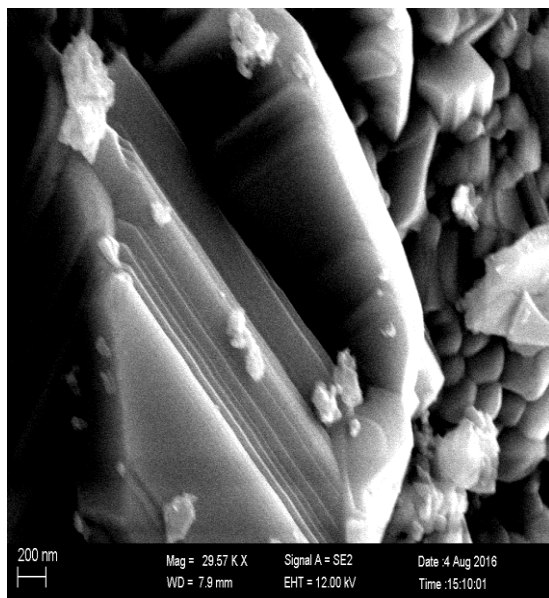
Morphological analysis of BLFSO nanostructure was done by using the scanning electron microscope (SEM) and is shown in Figures 4.6. SEM results shows that for first sample in which only (8%) La is doped in BFO, the nanosheets formation trend at its initial stage which increases with increase in the Se concentration. For 10% Se doping in BLFO by keeping the La value fixed, SEM results show the formation of intermediate phase between nanosheets and nanoparticles. Nanosheets formation increases by increasing the concentration of Se. The partial and complete nanosheets formation is seen for Se doping of 25% and 50 %, respectively, the fine nanosheets are formed and can be clearly seen in the SEM pictures. Here, the nanosheets are broken down to the lower dimensions upon 100% addition of Se in BLFO indicating that the self-accumulation of nanosheets into the flower-like structure is absent here.



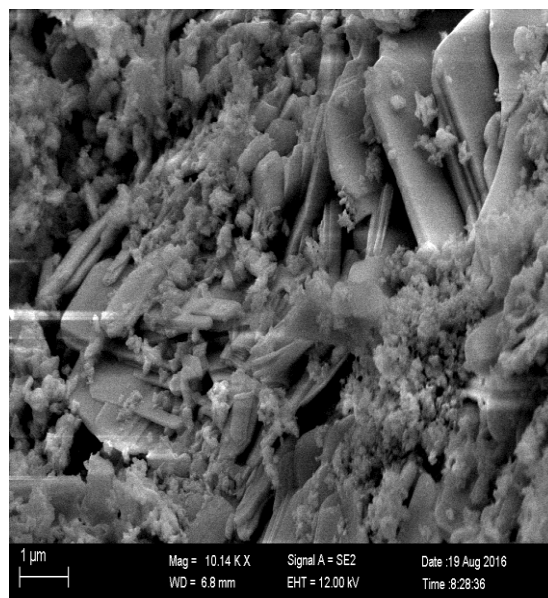
a) BLFO



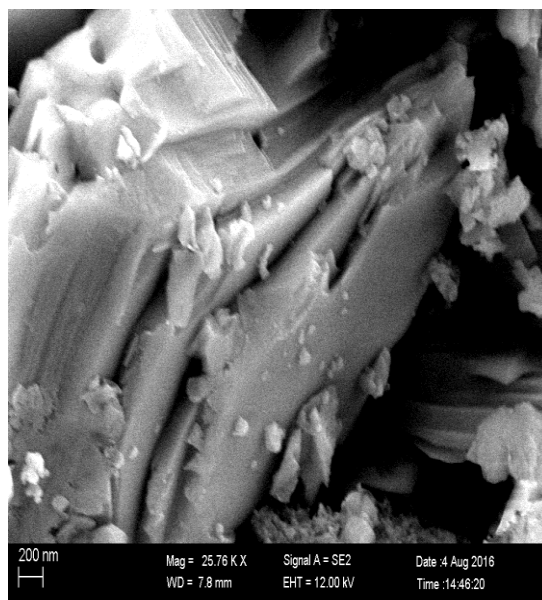
b) BLFSO-10



c) BLFSO-25



d) BLFSO-25



e) BLFSO-100.

Figure 4.6. The SEM images of (a) BLFO, (b) BLFSO-10 (c) BLFSO-25 (d) BLFSO-50

(e) BLFO-100

4.2.3 Magnetic properties of BLFSO

Figure 4.7 shows the M–H curves of BLFSO nanocomposites for different Se concentration at fixed La (0.08) concentration. The magnetization, remanent magnetization, and coercivity values are given in Table 2. Here the maximum magnetic moment increases from 0.052 emu/g (pure BFO) to 0.351 emu/gm for 8% doping of Lanthanum in BFO. This sudden increase in the magnetization is due to the suppression of spin modeling structure by La doping. By introducing the Se at B site in BLFO also change the value of magnetization. When 10% Se is doped in BLFO, the value of magnetization is 0.17231 emu/g much greater than the value of pure BFO. This change in magnetization is caused by the substitution of Se in BLFO, which collapses the antiferromagnetic spin structure because of the different ionic radii of Se^{+4} and Fe^{+3} cations due to which the uncompensated magnetic spins increases resulting in an overall increase in the magnetization. Also, the periodicity of the spin cycloid is broken which can be seen as the decreased particle sizes below the critical value of 62 nm [59]. The difference in the atomic radii of substituted atoms effect the size of the unit cell which leads to the suppression of the spiral spin structure resulting in not only the structural transitions but also the appearance of net magnetization. By increasing the value of Se concentration above 10%, the net magnetization decreases as seen from the table. The atoms on the surface have truncated bonds with less coordination neighbors thus, their mutual exchange interactions are reduced and hence, the saturation magnetization decreases due to the disordered surface spins.

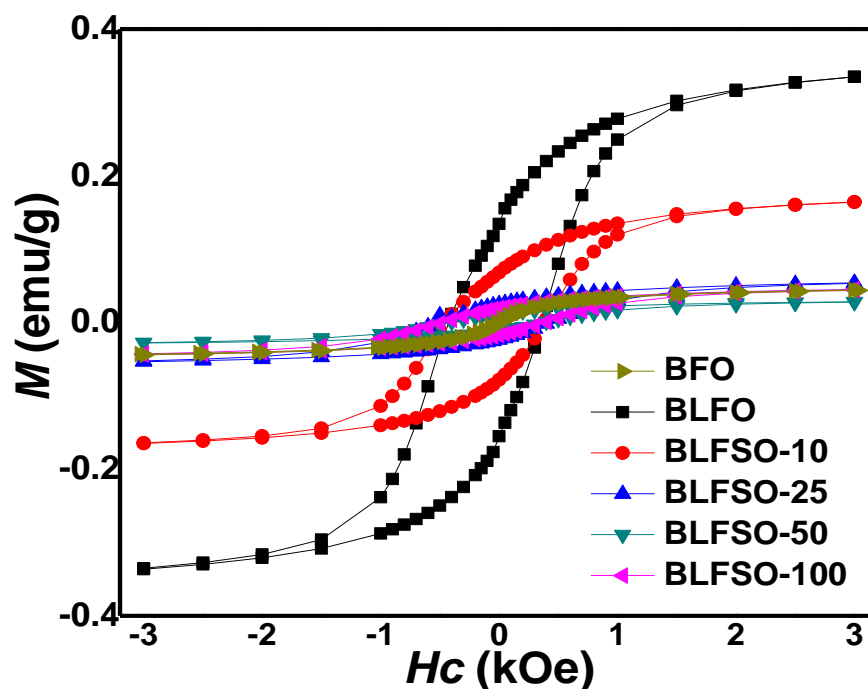


Figure4.7. Magnetization vs. field curves for BLFSO plotted at different Se-%.

| Sample | Mr (emu ⁻¹) | Ms (emu ⁻¹) | Hc (Oe) | Mr/Ms |
|-----------|-------------------------|-------------------------|---------|-------|
| BLFO | 0.1334 | 0.35198 | 432 | 0.37 |
| BLFSO-10 | 0.067 | 0.17231 | 434 | 0.38 |
| BLFSO-25 | 0.021 | 0.057 | 437 | 0.39 |
| BLFSO-50 | 0.011 | 0.0302 | 400 | 0.36 |
| BLFSO-100 | 0.019 | 0.0483 | 179 | 0.39 |

Table2. Table of magnetic parameters of Se substituted BLFO.

Figure4.8 shows coercivity values of the BLFSO nanoparticles which are higher than the pure BFO. At first, the coercivity for 10% of Se sample is 434Oe which increases further slightly to 437Oe upon increasing Se concentration to 25%. At 50% Se concentration, value goes to

437Oe. This increase in the value of H_c means our sample is becoming more and more magnetically harder but the change in coercivity is very small that shows that the formation of a mature nanostructure shape makes the magnetic domain structure fixed in placed. However, the coercivity decreases significantly to 179Oe for Se=100% which is due to the formation of smaller nanosheets resulting in better spin orientation for the given sample.

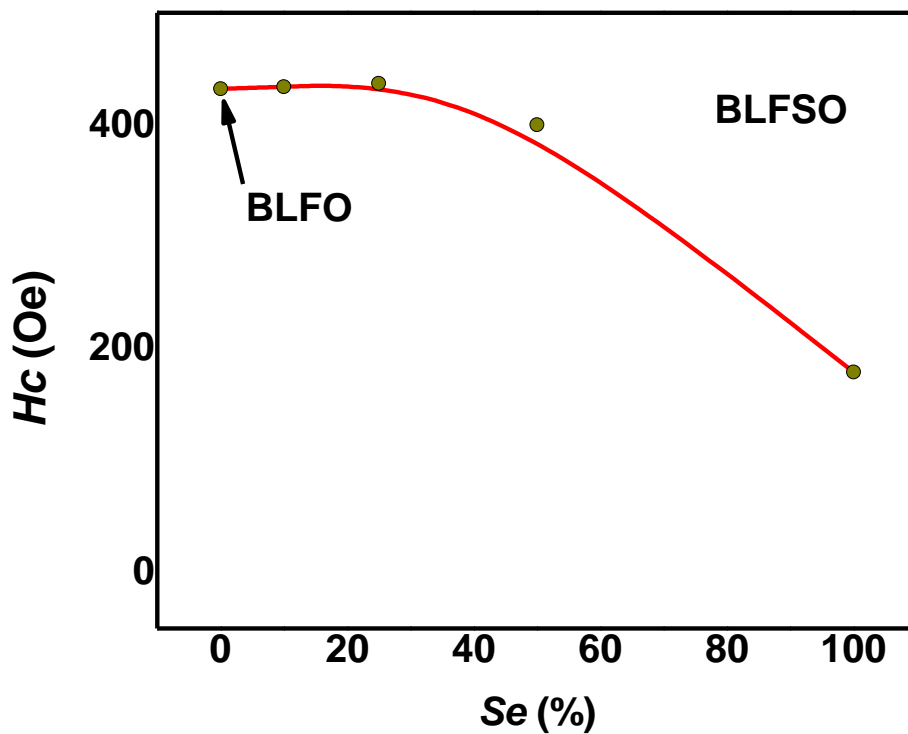


Figure4.8. The magnetic coercivity vs. Se-concentration for BLFSO.

Chapter 5 Result and Discussion

5.1. Photocatalytic Activity of Pure BLFSO

The photocatalytic activity of a series of BLFSO (Se=0%, 10%, 25%, 50%, 100%) nanoparticles were observed by checking the degradation of the model pollutant Congo Red (CR) aqueous solution under Uv-visible light. Pure BFO is less active for degradation of Congo red, but by introducing the dopent La and Se at A and B site in BFO respectively, photocatalytic activity is enhanced. Basically photocatalytic mechanism usually involve three steps i) absorption of photons ii) the production, separation of photo generated e^-h^+ pair iii) redox reactions. Selenium sites in BLFSO act as electron trapping sites that capture the excited electrons and promote the separation of e^-h^+ pair [60]. Actually, when the energy levels lie below the conduction bands edge, the excited electrons due to the photon absorption trapped. And when the energy level lie above the conduction band edge, electrons can quench the photo generated holes [61].

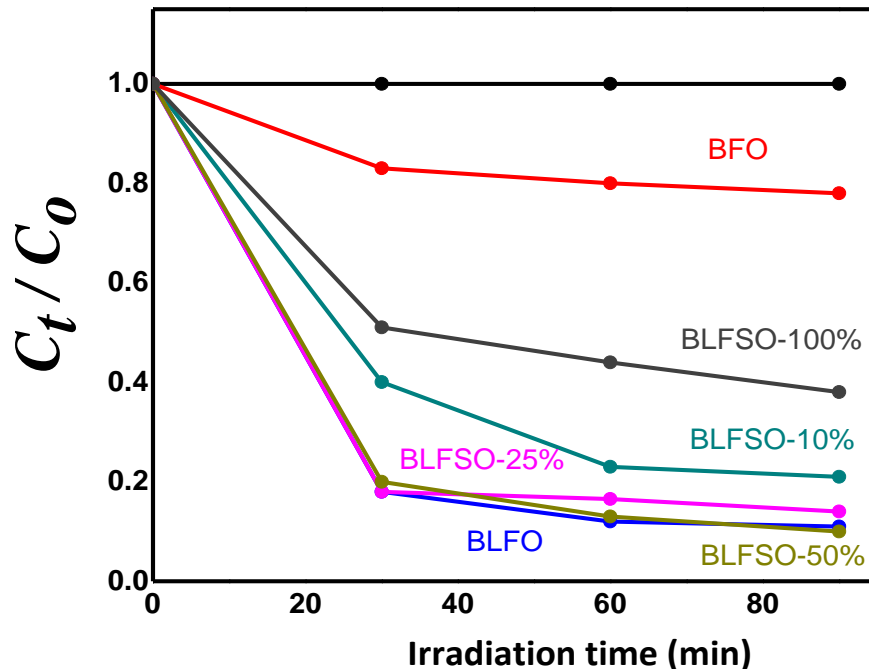


Figure 5.1. The photodegradation efficiencies of CR as a function of irradiation time under visible-light for BLFSO.

These photos generated e^-h^+ pairs took part in redox reactions and convert O^2 convert into $O^{\cdot-}$ radicals and H_2O into OH^\cdot for degradation of Congo Red.

Figure 5.1 shows that without any photocatalyst, less than 3% of CR is degraded after the exposure to Uv-visible irradiation for 90 minutes. With the addition of BFO as photocatalyst, over 20% of CR is degraded within the same length of irradiation time as shown in figure by red curve. With the doping of La in BFO, almost 93% of CR is degraded with the same 90 minutes time shown by blue line. For 10% Se doping in BLFO, 78% of CR is degraded shown by greenish curve. For 25% Se doping, almost 85% of CR is degraded but by increasing the concentration of Se, degradation decreased and only 58% of CR is degraded for 100% Se doping shown by Turquoise color.

The origin of enhanced photocatalytic performance in BFO is increased surface area and low recombination rate of charge carries after doping in BFO. As the surface area of photocatalyst increases, organic dyes are in direct contact with catalyst and easily redox reactions occurred. In BLFSO band gap is significantly reduced from [2.04 to 1.76 eV] for BLFSO-50%. As band gap is decreased the electrons can easily transferred from valence to conduction band and hence photocatalytic activity is increased due to good transport of charge carriers. From figure 5.1, the photocatalytic performance of doped samples increases at initial concentration, but decrease at higher concentrations of Se. By increasing the number of dopent, the average distance between trap sites decreases and causes a large re combination rate. This phenomena decrease the photocatalytic activity [62].

Figure 5.2 shows the absorption band gap of BFO and BLFSO. The band gap determined from absorption spectrum are 2.06 eV, 1.94 eV, 1.92 eV, 1.84 eV, 1.77 eV and 1.97 eV for BFO, BLFO, BLFSO-10%, BLFSO-25%, BLFSO-50%, BLFSO-100% respectively. Band gap value of BLFO is smaller than pure BFO and it could be attributed to a lattice strain effect by La doping in BFO. But by doping the Se in BLFO, the band gap value increases and reaches to the value of 1.97 eV for BLFSO-100. The absorption spectrum shows that for UV region (300-400 nm) BLFSO samples exhibits almost the same absorption behavior but this absorption is less than pure BFO. In the visible range (400-800 nm) all samples of BLFSO show higher absorption except BLFSO-100.

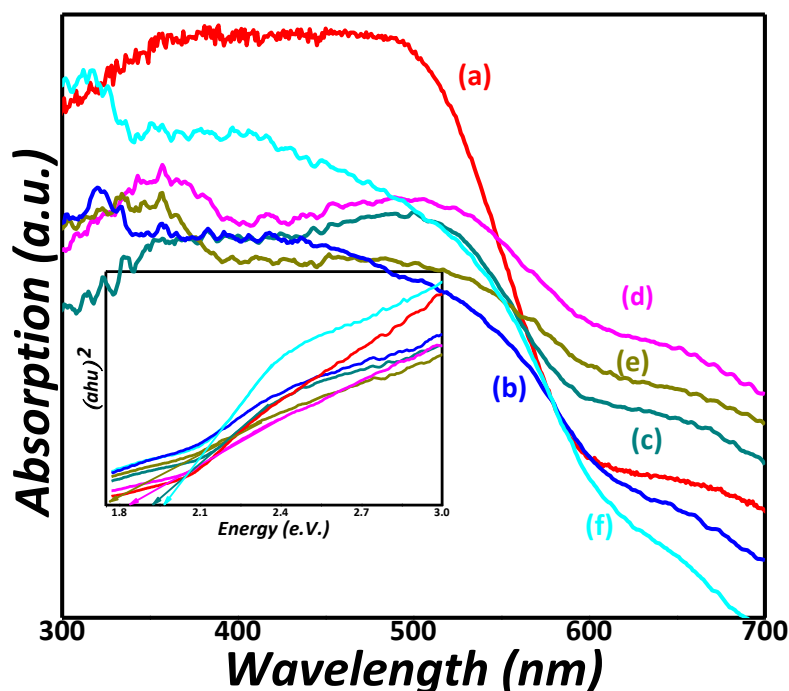


Figure 5.2. Optical absorption spectra of BLFSO samples; the inset shows the calculated band-gaps of BFO and BLFSO.

5.1.2 Photoluminescence spectra of Pure Samples BLFSO.

Figure 5.3 displays the PL spectra of the pure BiFeO_3 and the $\text{Bi}_{0.92}\text{La}_{0.08}\text{Fe}_{1-x}\text{Se}_x\text{O}_3$ nanoparticles. The main emission peak is at about 378nm for the pure BiFeO_3 sample. Compared with BiFeO_3 , the PL spectra intensity of the Selenium doped BLFO at different concentrations of Selenium is significantly decreased at the same position, which correspond that the charges recombination rate in BLFSO samples were much lower than that in BiFeO_3 samples. In general, the lower the charge recombination rate gives lower PL intensity and gives higher photocatalytic activity.

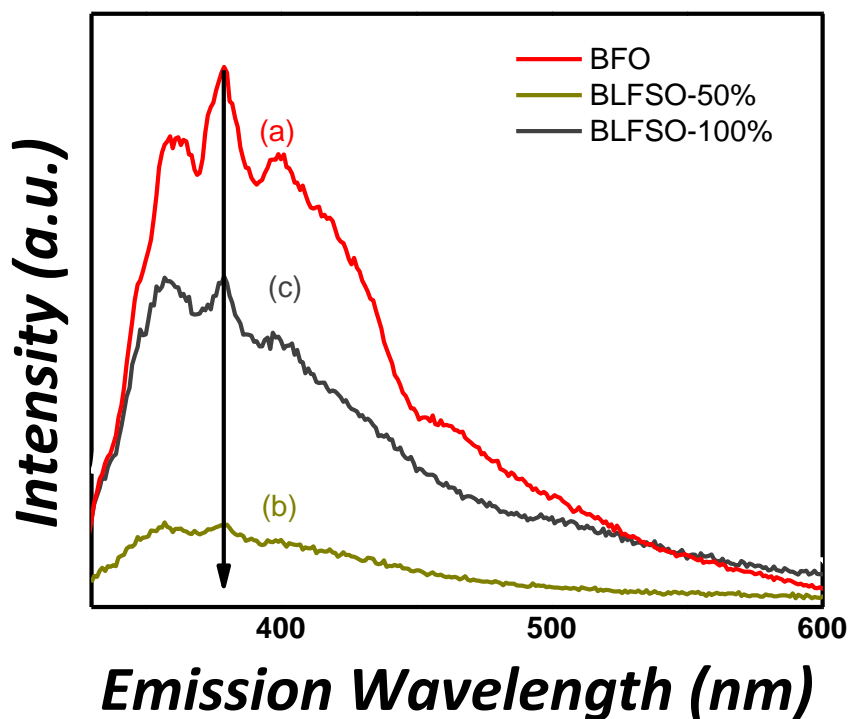


Figure 5.3. PL spectra of (a) BFO (b) BLFSO-25% (c) BLFSO-50% (d) BLFSO-10%

In figure 5.3 the red line shows the PL spectra of pre BFO samples. The higher values of intensity for BFO sample show that there is high charge recombination rate and therefore less photocatalytic activity. In figure the blue curve (a) has the lowest values corresponding to the lower values of charge recombination. This lower charge recombination rate of charge carrier increases the photocatalytic activity. This blue graph is referred to the $\text{Bi}_{0.92}\text{La}_{0.08}\text{Fe}_{0.9}\text{Se}_{0.10}\text{O}_3$. This sample shows the highest photocatalytic activity of 22 % and overall degradation of 80%. Similarly (b) and (c) graphs in the figure show the PL spectra for 25% and 50% doping in $\text{Bi}_{0.92}\text{La}_{0.08}\text{FeSO}_3$ respectively. (b) Curve shows the photocatalytic activity of 3% with overall degradation of 85%. (c) Curve shows the photocatalytic activity of 8% as it got lower position in the PL spectra. This sample shows the overall degradation of 90%.

5.2. Photocatalytic Activity of BLFSO/GO

5.2.1 XRD of BLFSO/GO Nanohybrids

Figure 5.4 illustrates the XRD patterns of BLFSO with GO monohybrids. All the XRD patterns are analyzed according to JCPDS card no. 20-0169. From the XRD data, there is a peak shift related to the (104) and (110) planes towards the lower angles similar as seen in the XRD of pure BLFSO. XRD pattern of hybrids show that the impurity phase peaks become short. It is due to the fact that the heat treatment at high temperature increases the crystallinity of hybrid samples. The intensity peak of (006) plane at 39° which arises from rhombohedral structure became weaker by increasing the Se concentration. This result showed the phase transformation from rhombohedral to orthorhombic phase. The results show that there is no extra peak obtained by the coating of GO on BLFO.

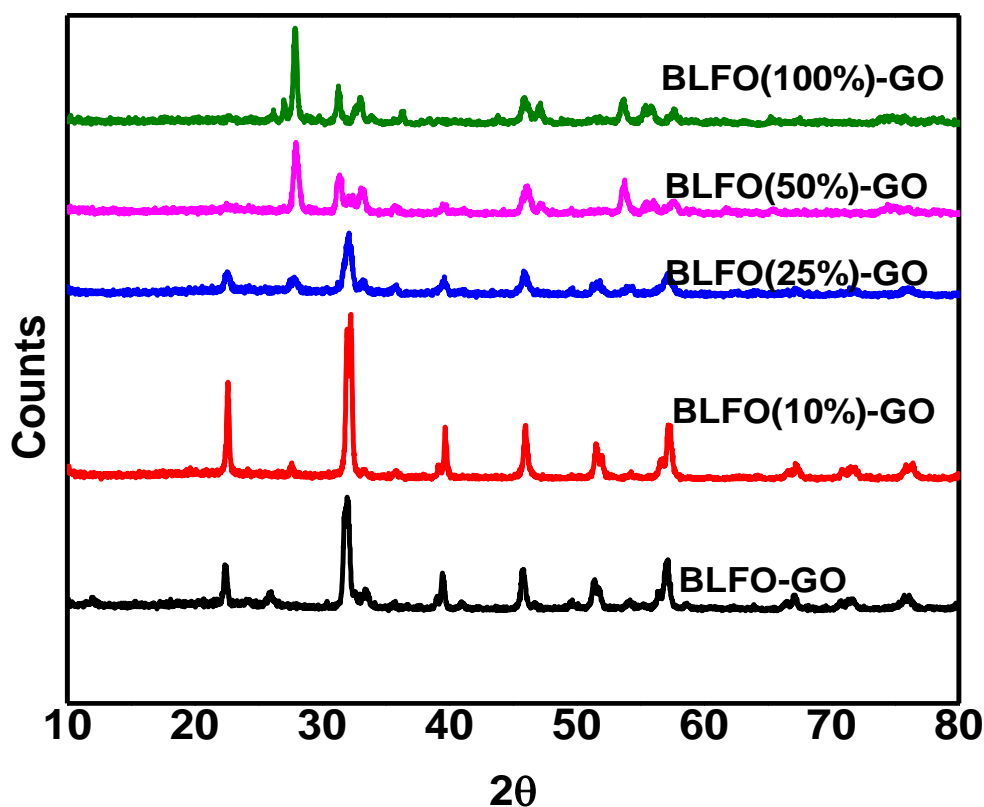
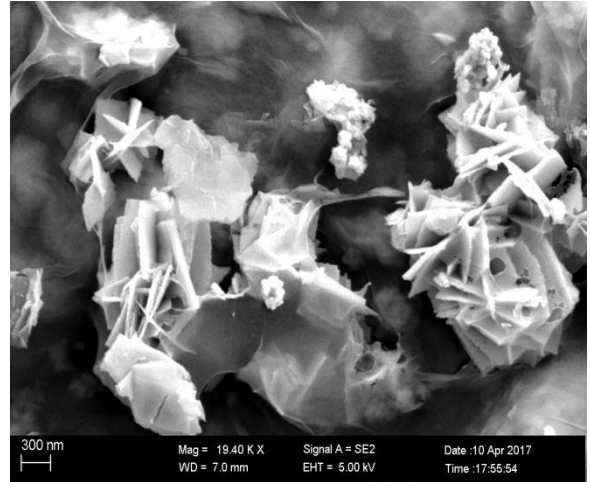
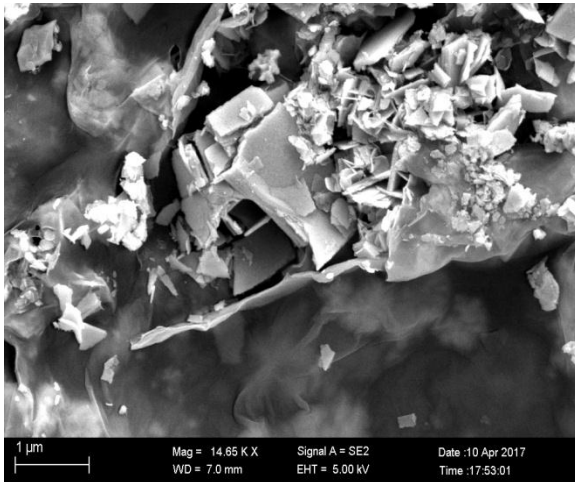


Figure 5.4 XRD pattern of hybrid sample of GO and BLFSO at different concentrations of Selenium.

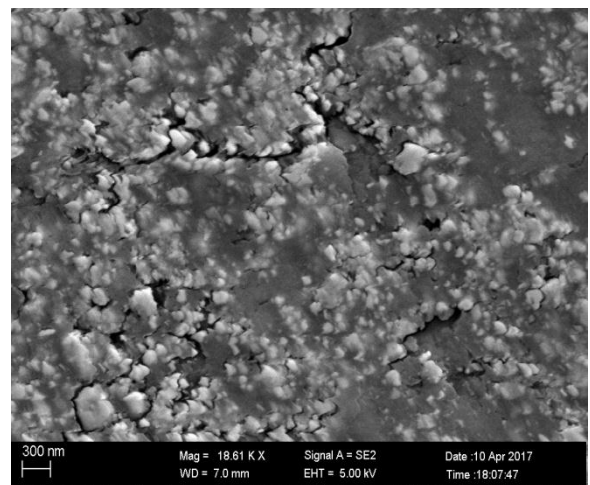
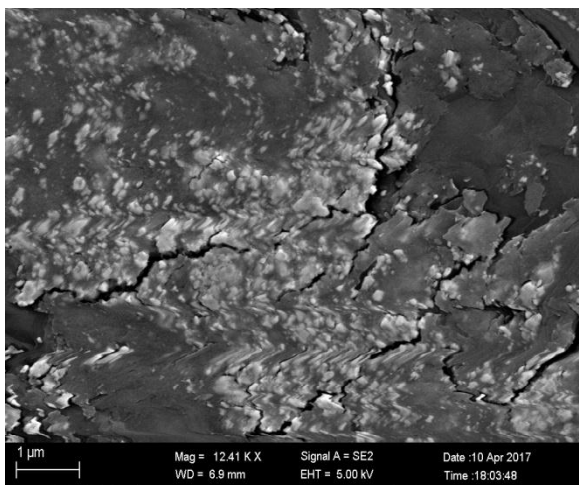
5.2.2 SEM images of BLFSO Hybrids

The morphology of BLFSO nano hybrids with graphene oxide was studied using Scanning electron microscope. Fig.5.5 shows scanning electron microscope images of nano hybrids. It can be seen that the nanoparticles of BLFSO have different particle morphologies and they are really integrated and dispersed on the surface of GO sheets. Particles and different nanosheets are covered with GO. Figures show that more and more nanoparticles of sample are located on the surface of graphene oxide as the concentration of Selenium increases in the sample. The nanoparticles are randomly attached to the surface of GO nanosheets which resemble crumpled silk veil waves as can be seen from the SEM images. These different types of morphology affect the process of photo catalysis significantly.

a)



b)



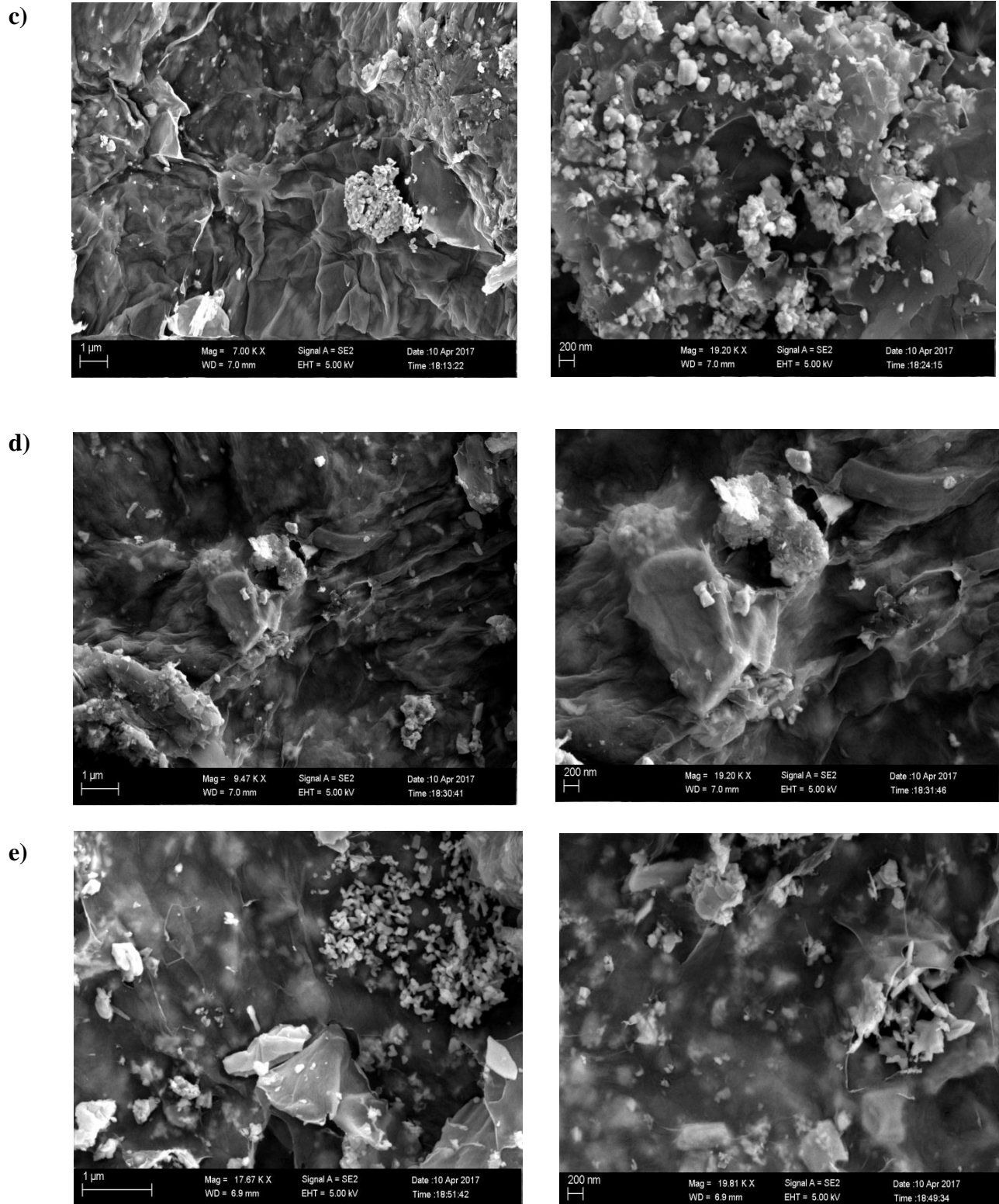


Figure 5.5. SEM images of (a) BLFSO-GO (b) BLFSO-10%-GO (c) BLFSO-25%-GO (d) BLFSO-50%-GO (e) BLFSO-100%-GO

5.2.3 X-ray Photoelectron spectra of (BLFSO/Go) Nanohybrids.

The XPS spectrum is used to investigate the chemical composition and surface state. The figure 5.6 shows the spectra of BLFSO/GO hybrids. From figure it can be seen that a binding energy peak appeared at 59 eV which attributed to Se^{+4} . Figure shows the binding energies at 158.8 eV and 163.9 eV for $\text{Bi}4f_{7/2}$ and $\text{Bi}4f_{5/2}$ respectively which are assigned to the Bi^{+3} . The two main peaks positioned at 711 eV and 726 eV are the $2p_{3/2}$ and $2p_{1/2}$ of Fe^{+3} [63]. The peak positioned at 532.8 eV corresponding to the O 1s spectrum. The binding energy of O 1s in the range of 53-532 eV was assigned to surface adsorbed oxygen. There are two peaks of carbon as shown in figure. First peak positioned at 285 eV shows the presence of C-C bond and second peak positioned at 286.9 eV shows the O-C. These results from XPS show the presence of oxygen and carbon atoms. It can be seen from XPS analysis that there is no existence of C-Fe.

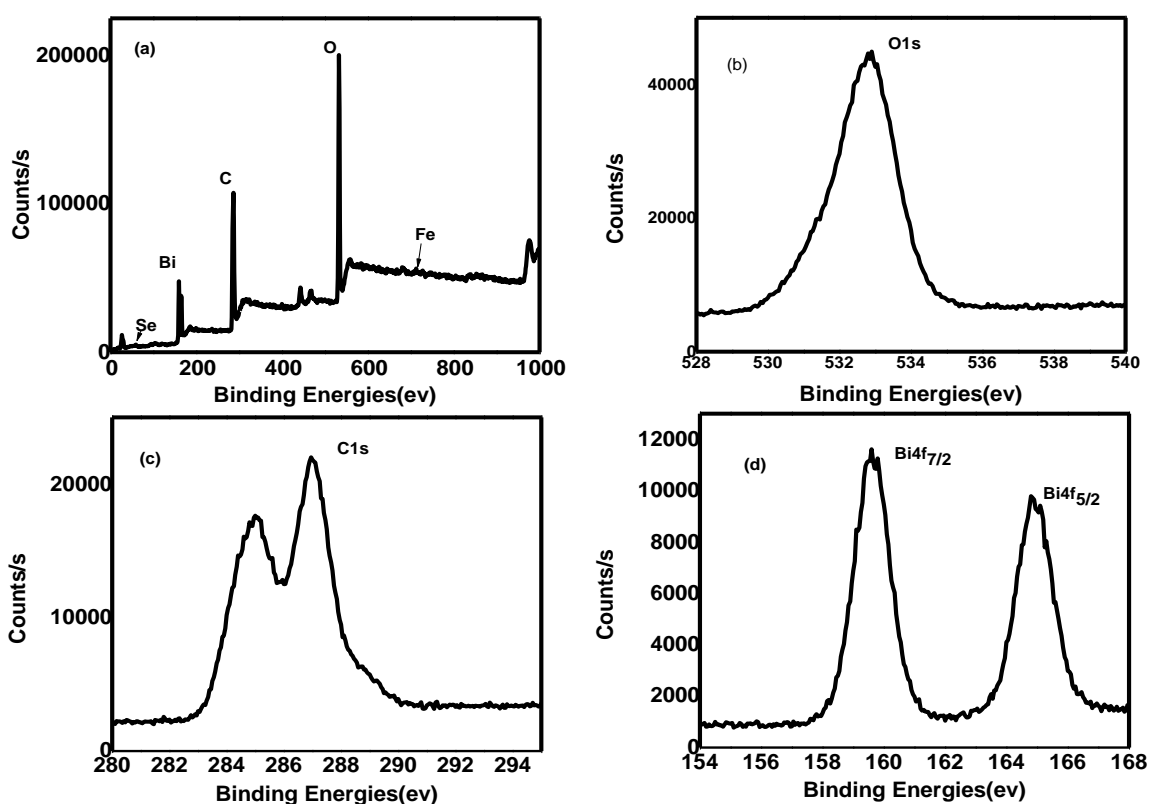


Figure 5.6 (a) XPS survey spectra of Se doped BLFO and high resolution spectra of (b) O 1s, (c) C 1s (d) Bi 4f and.

5.2.4 Photoluminescence spectra of BLFSO/GO Hybrid Samples.

Figure 5.7 shows the PL spectra of BLFSO/GO hybrid samples. The blue graph shows the PL spectra of BLFSO/GO sample without any concentration of Selenium. This Selenium free sample shows the photocatalytic of 6% with overall photodegradation of 70%. The higher values of Selenium concentration in hybrid samples change their PL spectra. The red graph shows the PL spectra of BLFSO/GO sample with 10% concentration of Selenium. This 10% Selenium sample shows the photocatalytic of 7% with overall degradation of only 15% as seen from the photocatalytic graphs of hybrid samples. The third graph in the figure shows the PL spectra of pre BLFSO/GO sample 100% concentration of Selenium. PL spectra of this sample shows the lowest value corresponding to the higher efficiency of Photocatalysis. This lower value of PL spectra correspond the lower charge recombination rate of charge carrier that increases the photocatalytic activity. It can be seen that the main emission peak is centered at about 430nm for the all hybrid samples. As compared to the pure samples, hybrid samples show lower photocatalytic activities due to high charge recombination of charge carriers in the hybrids sample.

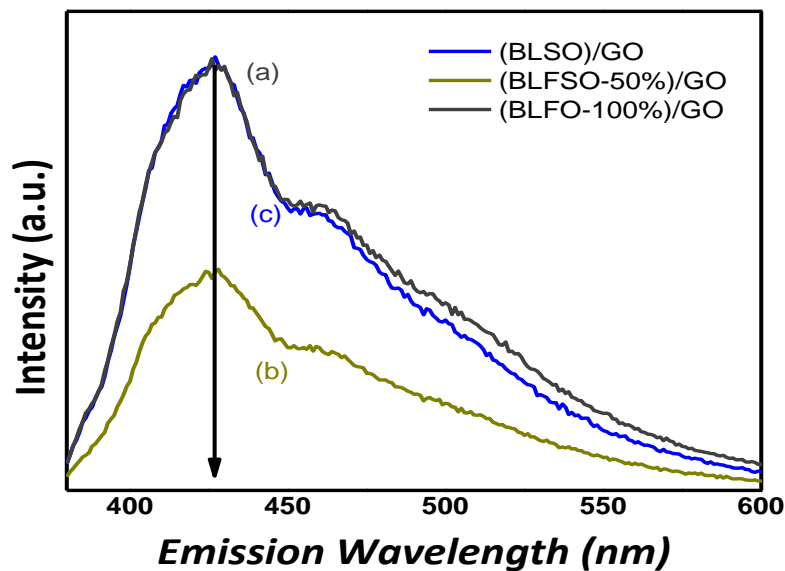


Figure 5.7. PL spectra of Hybrid sample of GO with (a) BLFSO-100% (b) BLFSO-100%)

(c) BLFSO-100%

5.2.5 Photocatalytic activity of Hybrid Samples

Figure 5.8 shows that when simple BFO was used as photocatalyst almost 20% of CR is degraded after the exposure to Uv-visible irradiation for 90 minutes. By using of BLFO hybrid with GO as photocatalyst, over 72% of CR is degraded within the same length of irradiation time 90 minutes as shown in figure by blue curve. In this sample 66% degradation is due to the adsorption of dye material on the sample and the photocatalytic activity is just 6%. For the hybrid sample of 10% Se doped in BLFSO and GO, 12% of CR is degraded shown by greenish curve and this abrupt decrease in the degradation efficiency is due to the low adsorption of only 5% and low photocatalytic activity of only 7% under light. For 25% Se doped hybrid sample, almost 50% of CR is degraded. By increasing the concentration of Se to 50% in BLFSO and GO sample, once again degradation efficiency decreases to the 79%. In this 50% Selenium doped sample, adsorption values once again increase to the value up to 77% with photocatalytic value of 2%. For 100% Se doped hybrid sample, 80% of CR is degraded as shown by Turquoise color. In this sample, photocatalytic activity is 18% with adsorption value of 61%.

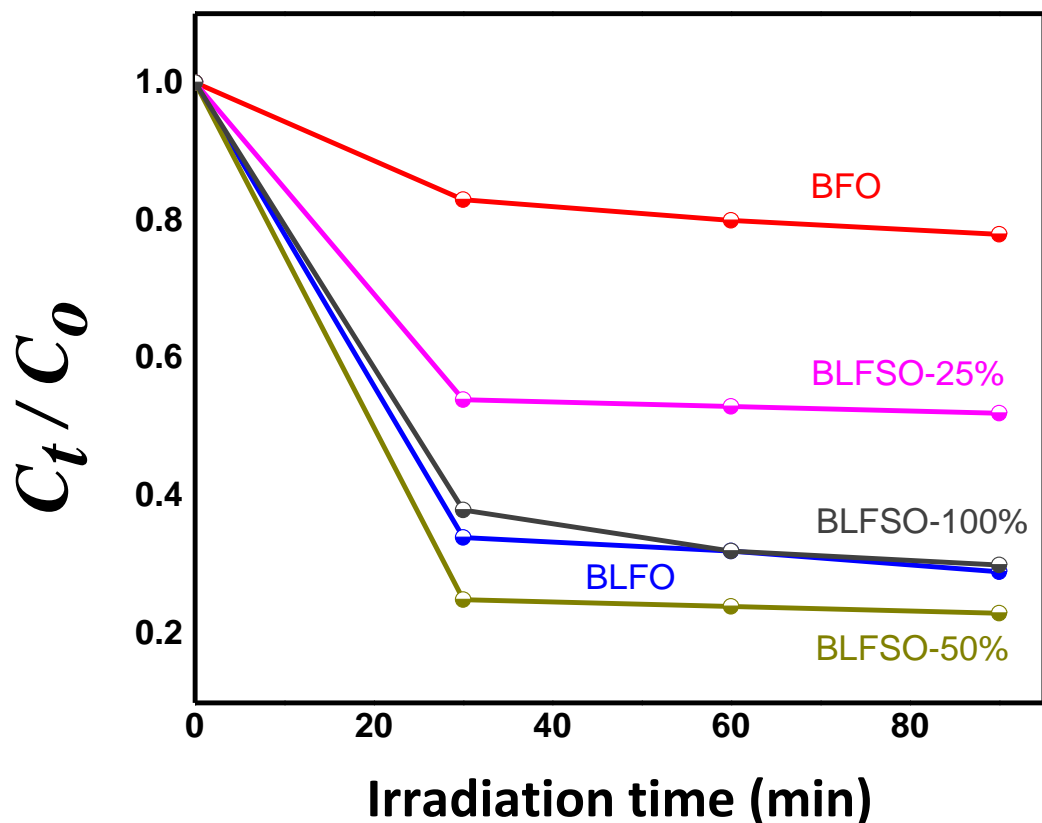


Figure 5.8. The photodegradation efficiencies of CR as a function of irradiation time Under visible-light for BLFSO-GO.

As compared to the pure samples of BLFSO (Se=0%, 10%, 25%, 50%, 100%), the photocatalytic activity decreases significantly for hybrid samples. Graphene oxide (GO) played an important role to change the photocatalytic activity of hybrid samples. In literature it is reported that good electron mobility capability of RGO helps to decrease the charge recombination rate and increase the value of photocatalytic. But in GO, there are some defect sites due to the presence of ep oxide, phen oxide and carboxylic acids on its surface. So GO behaves like electrical insulator. In our hybrid sample the photocatalytic activity decreases as compared to the pure samples, show that the reduction of Go to rGO to restore its electrical properties is not good enough for charge transfer and for electron trap [64].

To calculate the reduction of RGO, the oxygen-bound carbon content in RGO was measured by the following equation listed below:

$$\text{O-bound C \%} = (A_{\text{C-O}} + A_{\text{O-C=O}})/(A_{\text{C-C}} + A_{\text{C-O}} + A_{\text{O-C=O}}) \times 100\%.$$

Where $A_{\text{C-C}}$, $A_{\text{C-O}}$, and $A_{\text{O-C=O}}$ are the peak areas in the XPS spectra for the sp²-hybridized (C-C) and O-bound (C-O and O-C=O) carbon, respectively [65]. These calculations shows that reduction of GO to rGO is very low. It is found that the O-bound C content decreased from the original 55% in GO to approximately equal to 52% in the hybrid sample, indicating the a low reduction degree. The low reduction means the inefficient charge transfer and transportation of photogenerated charges. This inefficient charge transfer and charge trap will increase the rate of recombination of charges and cause to decrease the photocatalytic activity. In these samples the overall degradation is due to the adsorption. Only final sample in which 100% Se is doped shows 18% photocatalytic activity.

References

- [1] T.Pardeep, "A Textbook of Nanoscience and Nanotechnology", McGraw Hill Education Private Limited, New Delhi 2012.
- [2] Taniguchi, Norio. "On the basic concept of nano-technology." *Proc. Intl. Conf. Prod. London, 1974*. British Society of Precision Engineering, 1974.
- [3]Gribbin, John; Gribbin, Mary (1997). *Richard Feynman: A Life in Science*. Dutton. p. 170. ISBN 0-452-27631-4.
- [4] www.nanowerk.com/nanotechnology/ten_things_you_should_know_3.php
- [5] Buzea, Cristina, Ivan I. Pacheco, and Kevin Robbie. "Nanomaterials and nanoparticles: Sources and toxicity." *Biointerphases* 2.4 (2007): MR17-MR71..
- [6] http://events.nace.org/TCCNews/2ndQuarter_2014/images/nanomaterialsclassification.jpg
- [7] Tiwari, Jitendra N., Rajanish N. Tiwari, and Kwang S. Kim. "Zero-dimensional, one-dimensional, two-dimensional and three-dimensional nanostructured materials for advanced electrochemical energy devices." *Progress in Materials Science* 57.4 (2012): 724-803.
- [8] Peng, Xu, et al. "Two dimensional nanomaterials for flexible supercapacitors." *Chemical Society Reviews* 43.10 (2014): 3303-3323.
- [9] <http://eu.wiley.com/WileyCDA/WileyTitle/productCd-3527337806.html>
- [10] David K. Ferry, Stephen M. Goodnick and Jonathan Bird, *Transport in Nanostructures*, Cambridge University Press, 2009.
- [11] <http://www.bbc.co.uk/staticarchive/1ba786c30a635037b6a1fc3d8a992d477c68bbc9.jpg>
- [12] B. Kramer, T. Brandes, W. Hausler, K. Jauregui, W. Pfaff and D. Weinmann, "Interactions and transport in nanostructures", 1994, 1871-1878
- [13] Goldman, A. (1990). *Modern Ferrite Technology*. Van Nostrand Reinhold, New York.
- [14] Callister, W. (2003). *Materials science and engineering an introduction*. Sixth ed. New York: JoHn Wiley & Sons, Inc.

- [15] Spaldin, N. (2003). *Magnetic materials: Fundamentals and device applications*. Cambridge: Cambridge University press.
- [16] Cullity, B. D. (1978). *Introduction to Magnetic Materials* (2nd ed.). Addison-Wesley Publishing.
- [17] Schmid H.J *Phy: Cond Matter* 2008;20:434201-25
- [18] Reddy, V. Annapu, N. P. Pathak, and R. Nath. "Particle size dependent magnetic properties and phase transitions in multiferroic BiFeO₃ nano-particles." *Journal of Alloys and Compounds* 543 (2012): 206-212.
- [19] Filippetti A, Hill NA. *Phys Rev B* 2002;65:195120e30.
- [20] Benjamin Ruetter, S. Zvyagin, A.P. Pyatakov, A. Bush, J.F. Li, V.I. Belotelov, A.K. Zvezdin, D. Viehland, *Phys. Rev. B* 69 (2004) 064114.
- [21] https://www.intechopen.com/source/html/44929/media/image4_w.jpg
- [22] Palkar VR, Pinto R. *Pramana J Phys* 2002;58:1003e8.
- [23] Reddy, V. Annapu, N. P. Pathak, and R. Nath. "Particle size dependent magnetic properties and phase transitions in multiferroic BiFeO₃ nano-particles." *Journal of Alloys and Compounds* 543 (2012): 206-212.
- [24] Park, Tae-Jin, et al. "Size-dependent magnetic properties of single-crystalline multiferroic BiFeO₃ nanoparticles." *Nano letters* 7.3 (2007): 766-772.
- [25] Jarrier, R., et al. "Surface phase transitions in BiFeO₃ below room temperature." *Physical Review B* 85.18 (2012): 184104.
- [26] Fischer, P., et al. "Temperature dependence of the crystal and magnetic structures of BiFeO₃." *Journal of Physics C: Solid State Physics* 13.10 (1980): 1931.
- [27] Catalan, Gustau, and James F. Scott. "Physics and applications of bismuth ferrite." *Advanced Materials* 21.24 (2009): 2463-2485.
- [28] Wang, Yonggang, et al. "Hydrothermal synthesis of single-crystal bismuth ferrite nanoflakes assisted by potassium nitrate." *Ceramics International* 35.3 (2009): 1285-1287.

- [29] Ghosh, Sushmita, et al. "Low temperature synthesis of bismuth ferrite nanoparticles by a ferrioxalate precursor method." *Materials research bulletin* 40.12 (2005): 2073-2079.
- [30] Wang, Yonggang, et al. "Low temperature polymer assisted hydrothermal synthesis of bismuth ferrite nanoparticles." *Ceramics International* 34.6 (2008): 1569-1571.
- [31] Chen, Chao, et al. "Hydrothermal synthesis of perovskite bismuth ferrite crystallites." *Journal of Crystal Growth* 291.1 (2006): 135-139.
- [32] Cao, Ling-Fei, et al. "Size and shape effects on Curie temperature of ferromagnetic nanoparticles." *Transactions of Nonferrous Metals Society of China* 17.6 (2007): 1451-1455.
- [33] Zhang, Ziang, et al. "Influence of La doping on magnetic and optical properties of bismuth ferrite nanofibers." *Journal of Nanomaterials* 2012 (2012): 4.
- [34] Sharma, Poorva, Ashwini Kumar, and Dinesh Varshney. "Rare earth (La) and metal ion (Pb) substitution induced structural and multiferroic properties of bismuth ferrite." *Journal of Advanced Ceramics* 4.4 (2015): 292.
- [35] Cheng, Z. X., et al. "Structure, ferroelectric properties, and magnetic properties of the La-doped bismuth ferrite." *Journal of Applied Physics* 103.7 (2008): 07E507.
- [36] García-Zaldívar, O., et al. "BiFeO₃ codoping with Ba, La and Ti: Magnetic and structural studies." *Journal of Advanced Dielectrics* 5.04 (2015): 1550034.
- [37] Irfan, Syed, et al. "Mesoporous template-free gyroid-like nanostructures based on La and Mn co-doped Bismuth ferrites with improved photocatalytic activity." *RSC Advances* 6.115 (2016): 114183-114189.
- [38] Liu, Ting, Yebin Xu, and Jingyuan Zhao. "Low-Temperature Synthesis of BiFeO₃ via PVA Sol-Gel Route." *Journal of the American Ceramic Society* 93.11 (2010): 3637-3641.
- [39] Lv, Yuepeng, et al. "The effect of solvents and surfactants on morphology and visible-light photocatalytic activity of BiFeO₃ microcrystals." *Journal of Materials Science. Materials in Electronics* 26.3 (2015): 1525.

- [40] Zhang, Yu-jie, et al. "Structural and magnetic properties in Bi 1- x R x FeO 3 (x= 0-1, R= La, Nd, Sm, Eu and Tb) polycrystalline ceramics." *Journal of Magnetism and Magnetic Materials* 322.15 (2010): 2251-2255.
- [41] Chen, Zhiwu, et al. "Ferromagnetic and photocatalytic properties of pure BiFeO₃ powders synthesized by ethylene glycol assisted hydrothermal method." *Journal of Materials Science. Materials in Electronics* 26.2 (2015): 1077.
- [42] Chauhan, Sunil, et al. "Structural, vibrational, optical, magnetic and dielectric properties of Bi 1- x Ba x FeO 3 nanoparticles." *Ceramics International* 39.6 (2013): 6399-6405.
- [43] Tang, Ping, et al. "The structural, optical and enhanced magnetic properties of Bi 1- xGdxFe 1- yMnyO 3 nanoparticles synthesized by sol-gel." *Journal of Alloys and Compounds* 622 (2015): 194-199.
- [44] Arya, G. S., R. K. Kotnala, and N. S. Negi. "Enhanced magnetic and magnetoelectric properties of In and Co codoped BiFeO₃ nanoparticles at room temperature." *Journal of nanoparticle research* 16.1 (2014): 1.
- [45]http://eresources.gitam.edu/nano/NANOTECHNOLOGY/role_of_bottomup_and_topdown_a.htm
- [46] L. Klaus-Dieter; Bartels, Arno; Schreyer, Andreas; Clemens, Helmut, "High-Energy X-Rays: A tool for Advanced Bulk Investigations in Materials Science and Physics". Textures and Microstructures, 2003, 219.
- [47] <http://www.microscopy.ethz.ch/bragg.htm>
- [48] <http://chemistry.tutorvista.com/nuclear-chemistry/x-rays.html>
- [49] D, McMullan, "Scanning Electron Microscopy", 2006, 1928.
- [50] <http://www.ammrf.org.au/myscope/sem/background/concepts/interactions.php>
- [51] <https://www.purdue.edu/ehps/rem/rs/sem.htm>
- [52] A. Misra, B. Prabhakar, "Ultraviolet Spectroscopy and UV laser", Newyork, Marcel Dekker, 2002.
- [53] Swinehart, D. F. "The beer-lambert law." *J. Chem. Educ* 39.7 (1962): 333.
- [54] http://faculty.sdmiramar.edu/fgarces/labmatters/instruments/uv_vis/cary50.htm

- [55] Irfan, Syed, et al. "The gadolinium (Gd 3+) and Tin (Sn 4+) Co-doped BiFeO₃ nanoparticles as new solar light active photocatalyst." *Scientific Reports* 7 (2017): srep42493.
- [56] S. Irfan, S. Rizwan, Y. Shen, R. Tomovska, S. Zulfiqar, M. I. Sarwar, and C.-W. Nan, *RSC Ad*, 2016, 6, 114183-114189.
- [57] T. J. Park, G. C. Papaefthymiou, A. J. Viescas, A. R. Moodenbaugh, and S. S. Wong, *Nano Letters*, 2007, 7, 766-772.
- [58] S. Michea, J. L. Palma, R. Lavín, J. Briones, J. Escrig, J. C. Denardin, and R. L. Rodríguez-Suárez, *Journal of Physics D: Applied Physics*, 2014, 47, 335001.
- [59] K. Nadeem, H. Krenn, T. Traussnig, R. Würschum, D. V. Szabó, and I. Letofsky-Papst, *Journal of Magnetism and Magnetic Materials*, 2011, 323, 1998-2004.
- [60] Irfan, Syed, et al. "Enhanced photocatalytic activity of La 3+ and Se 4+ co-doped bismuth ferrite nanostructures." *Journal of Materials Chemistry A* 5.22 (2017): 11143-11151.
- [61] K. Nagaveni, M. S. Hegde, G. Madras, *J. Phys. Chem., B*, 2004, 108, 20204–20212.
- [62] W. Choi, A. Termina, M.R. Hoffman, *J. Phys. Chem.*, 1994, 98, 13669–13679.
- [63] Meng, Wanwan, et al. "Influence of lanthanum-doping on photocatalytic properties of BiFeO₃ for phenol degradation." *Chinese Journal of Catalysis* 37.8 (2016): 1283-1292.
- [64] Chen, Yongjuan, et al. "Reduction degree of reduced graphene oxide (RGO) dependence of photocatalytic hydrogen evolution performance over RGO/ZnIn₂S₄ nanocomposites." *Catalysis Science & Technology* 3.7 (2013): 1712-1717.
- [65] A. Iwase, Y. H. Ng, Y. Ishiguro, A. Kudo and R. Amal, *J. Am. Chem. Soc.*, 2011, 133, 11054–11057.